

Radiative shocks in galaxy formation. I: Cooling of a primordial plasma with no sources of heating.

M.I. Forcada-Miró^{1,2} and S.D.M. White²

¹*Institute of Astronomy, Madingley Road, Cambridge CB3 0HZ, England*

²*Max-Planck-Institut für Astrophysik, Karl-Schwarzschild-Straße 1, 85748 Garching b. München, Germany*

Accepted ????. Received ????

ABSTRACT

We use a 1-D Lagrangian code which follows both a gaseous and a dark component to study the radiative shocks that appear in the evolution of spherical scale-free perturbations in an Einstein-de Sitter Universe. The detailed behaviour of the shock depends on whether the radiative cooling is dominated by bremsstrahlung or line cooling. Bremsstrahlung is the main energy loss mechanism for systems with circular velocity $V_c > 100 \text{ km s}^{-1}$. In this case, we can reproduce the kinematics of the shock and of the cooling wave to a high degree of accuracy with a simple analytic model. When line cooling dominates, the shock front can be unstable to oscillations. The period and amplitude of the oscillations increase in time as the universe expands. For such systems, our analytic model provides only a rough estimate of the mean evolution. We believe that now we fully understand the effect radiative cooling has in the shocks that appear in spherical models for galaxy formation.

Key words: Cosmology: theory – galaxies: formation – hydrodynamics

1 INTRODUCTION

The origin of galaxies is still an open question in modern cosmology. The standard picture of structure formation supposes that the nonlinear objects we observe today grew through gravitational instability from a spectrum of linear primordial fluctuations (Peebles 1967). The cosmic microwave background radiation (CMB) can severely constrain such structure formation models (White, Scott & Silk 1994), but observations with high angular resolution are required to put direct constraints on scales approaching those relevant to galaxy formation. Cosmogonies dominated by cold dark matter (CDM) are the current standard, but there are few unambiguous tests of their predictions so far on galactic scales (Blumenthal *et al.* 1984; Davis *et al.* 1985; Ostriker 1993; Ostriker and Steinhardt 1995).

In a cold dark matter scenario structure forms hierarchically, which means that small objects form first and merge to form bigger ones. As the gas falls into the potential well of the forming halo it passes through a shock in which its bulk kinetic energy is converted into thermal energy. In the case when the gas can cool efficiently it will flow further in, getting very dense. This cold and dense gas in the innermost parts of halos provides suitable raw material for star formation. The important role of radiative cooling in structure formation was first pointed out independently by

Binney (1977), Rees & Ostriker (1977) and Silk (1977), and the way in which it leads to galaxy formation at the centres of dark matter halos was first described and modelled by White & Rees (1978). If we want to understand the formation of galaxies it is essential to study how the gas cools and settles in the central regions of dark matter halos.

Rapid improvements in computer technology have played an important role in the theory of structure formation, since numerical simulations can provide detailed quantitative predictions to be compared to real data. Until quite recently only the gravitational clustering of the collisionless component could be followed (e.g. Davis *et al.* 1985). Over the last few years, however, it has become feasible to introduce gas dynamics and cooling/heating processes in simulations of galaxy formation (e.g. Cen 1992; Katz, Hernquist & Weinberg 1992; Navarro & White 1993; Steinmetz 1996). Such three-dimensional simulations require a large amount of CPU-time, and as a result exhaustive parameter studies are difficult. Moreover, numerical artifacts often complicate interpretation of the results, and a clear picture of the physics behind the evolution of such simulations is not easy to build.

A very useful alternative is provided by semi-analytic models which combine an algorithm for predicting the abundance and merging of dark-matter halos (or alternatively a high resolution cosmological N-body simulation of this pro-

cess) with cooling arguments to prescribe galaxy condensation at halo centres, with a simple star formation law, and with parametrised models for supernova feedback and for spectrophotometric evolution; such models are ideal for parameter studies and for direct comparison with observation, and their quantitative predictions can agree reasonably well with a wide range of data (e.g. White & Frenk 1991; Kauffmann, White & Guiderdoni 1993; Cole *et al.* 1994; Kauffmann, Nusser & Steinmetz 1997).

On the other hand, semi-analytical models are only as good as the simple models they use for the various physical processes involved. One-dimensional numerical simulations are a potential tool to improve such models which do not suffer from many of the inconveniences of their three-dimensional counterparts. However, very little has been done in this direction since the pioneering work of Larson (1974). The formation and growth of plane-symmetric pancakes has been studied by Shapiro & Struck-Marcell (1984) and more recently by Anninos & Norman (1994); Thoul & Weinberg studied dissipational spherical collapses onto local density maxima of a primordial Gaussian density perturbation field (Thoul & Weinberg 1995) and the effects of a background of ultraviolet radiation (Thoul & Weinberg 1996); Haiman *et al.* (1996) adapted the code built by Thoul and Weinberg to investigate radiative cooling by molecular hydrogen. The present paper lies within this general framework and focusses on the study of the radiative shocks that appear in the evolution of spherical scale-free perturbations in an Einstein-de Sitter universe. It is organized as follows: in Section 2 we present our basic model for formation of a galaxy, as well as the 1D-Lagrangian code we use to study its evolution; in Section 3 we test the code against some existing solutions; in Section 4 we present the results of our simulations of galaxy formation; finally, in Section 5 we present physical explanations for the behaviour observed in the simulations.

2 MODEL AND NUMERICAL METHOD

The observed rotation curves of spiral galaxies and the orbital velocities of their satellites seem to indicate that the surrounding dark halos have an approximately isothermal profile $\rho \sim r^{-2}$ (e.g. Casertano & Van Gorkom 1991; Zaritsky & White 1994). An appropriate 1-D model for halo formation should build up such a halo through infall of material from an expanding universe. Gott (1975) and Gunn (1977) were the first to construct a model of this type. They considered accretion onto a central seed from an otherwise unperturbed universe, and showed that the resulting density profile had $\rho \propto r^{-9/4}$ for an Einstein-de Sitter background cosmology. By allowing a wider variety of scale-free initial perturbations Fillmore & Goldreich (1984) showed that a range of power law exponents (including -2) could be obtained. White & Zaritsky (1992) (thereafter WZ) extended these self-similar infall models in two ways. They showed how to embed them in an open universe and how the infalling particles could be given nonradial orbits. In the WZ model the initial specific binding energy of a shell is perturbed in the following way:

$$\delta E(M) = \delta E_o \left(\frac{M}{M_o} \right)^{\frac{2}{3} - \epsilon}, \quad (1)$$

where M is the mass initially inside the shell. A halo with a flat circular velocity curve near the centre results for $\epsilon = 2/3$. We use this particular case to generate our initial conditions.

2.1 Collisionless component

In the model of WZ the equations for the evolution of the collisionless component are:

$$\frac{d^2 r_i}{dt^2} = - \frac{G M_i r_i}{(r_i^2 + a^2)^{\frac{3}{2}}} - \frac{G M_i K_i J_i}{r_i^2} + \frac{J_i^2}{r_i^3}, \quad (2)$$

$$\frac{dJ_i}{dt} = G M_i K_i \frac{dr_i}{dt}, \quad (3)$$

$$G M_i K_i = \begin{cases} (-2E_i)^{\frac{1}{2}} \sqrt{\frac{1-e}{1+e}} & t \leq t_i \\ 0 & t > t_i \end{cases}, \quad (7)$$

$$M_i = \sum_{r_j < r_i} m_j, \quad (5)$$

where m_i , r_i , J_i and t_i are the masses, radii, specific angular momenta, and turnaround times of the shells, M_i is the total mass within shell i , and e , the eccentricity of the final orbit, is assumed to be the same for all shells (see WZ for more details).

In order to avoid a divergence of the gravitational acceleration near the origin the potential is softened in the usual way. By choosing an appropriate value of e we also give each shell enough angular momentum to prevent it from getting very close to the center. In most of our calculations we adopt $e = 0.7$ which results in almost isotropic velocity dispersions in the virialised regions of the halo.

We integrate equations (2-5) by means of the force-average method. First of all we predict new positions and velocities using the accelerations calculated at the beginning of the time-step f_i^n :

$$r_i^* = r_i^n + \Delta_{DM} t v_i^n + 0.5 \Delta_{DM}^2 f_i^n, \quad (6)$$

$$v_i^* = v_i^n + \Delta_{DM} f_i^n. \quad (7)$$

Now, with the predicted positions we can calculate accelerations at the end of the time step f_i^* and use a centred scheme to get positions and velocities for the beginning of the next step:

$$v_i^{n+1} = v_i^n + 0.5 \Delta_{DM} (f_i^n + f_i^*), \quad (8)$$

$$r_i^{n+1} = r_i^n + 0.5 \Delta_{DM} (v_i^n + v_i^{n+1}). \quad (9)$$

Finally we just set $f_i^{n+1} = f_i^*$ and the step is complete. With this scheme we only have to calculate the forces once per timestep. The timestep Δ_{DM} is taken as:

$$\Delta_{DM} = \min_i \left(C_{DM} \frac{a}{|v_i|} \right), \quad (10)$$

where $C_{DM} = 0.1$, so that no individual particle moves more than 10% the softening length in a timestep.

2.2 Gas component

The initial conditions for the gas are generated in the same way as for the dark matter but with no angular momentum. We integrate the usual hydrodynamic equations, which in spherical symmetry can be written in the Lagrangian form,

$$\frac{\partial m}{\partial r} = 4\pi r^2 \rho, \quad (11)$$

$$\frac{dv}{dt} = -4\pi r^2 \frac{\partial P}{\partial m} - \frac{4\pi}{r} \frac{\partial(r^3 Q)}{\partial m} - \frac{GM_t r}{(r^2 + a^2)^{3/2}}, \quad (12)$$

$$\frac{du}{dt} = -4\pi P \frac{\partial(r^2 v)}{\partial m} + \frac{3}{2} \frac{Q}{\rho} \left(\frac{\partial v}{\partial r} - \frac{\partial(r^2 v)}{\partial r^3} \right) + \frac{1}{\rho} (\Gamma - \Lambda), \quad (13)$$

$$Q = \begin{cases} 3l^2 \rho \frac{\partial(r^2 v)}{\partial r^3} \left(\frac{\partial v}{\partial r} - \frac{\partial(r^2 v)}{\partial r^3} \right) & \text{if } \frac{\partial(r^2 v)}{\partial r^3} < 0 \\ 0 & \text{otherwise} \end{cases}, \quad (13)$$

$$P = (\gamma - 1)\rho u, \quad (14)$$

where ρ , v , P and u are the gas mass density, velocity, pressure and specific internal energy of the gas, Λ the radiative cooling rate, Γ the photoionization heating rate, γ the ratio of specific heats, and M_t the total mass (gas and dark matter) inside the shell at radius r . In order to treat shocks accurately we have implemented the Tensor Artificial Viscosity scheme of Tscharnutter & Winkler (1979) (TAV). The artificial viscous pressure Q is only non-zero in regions that are undergoing compression (i.e. the divergence of the velocity field is negative), and converts bulk kinetic energy into internal energy over the scale height l , which is taken to be $l = \lambda \Delta r$, where Δr is the radial thickness of the shell. The parameter λ has to be big enough to damp out post-shock oscillations but small enough to have a good shock resolution. We have found that a value $\lambda = \sqrt{6}$ works well and smears the shock over six zones.

We set up a logarithmic grid in which equations (11–14) are discretized in the way prescribed by Benz (1991) (for details see Forcada-Miró 1997). Time integration is performed explicitly, except for the radiative processes, for which we switch between an explicit and an implicit method (see 2.3). In this way the timestep never becomes too small when strong cooling occurs, but still, the limitations on the timestep for the gas are stronger than for the dark matter. Consequently, we allow different timesteps for the two components. The timestep for the gas is taken as

$$\Delta t_g = \min(\Delta t_{CFL}, \Delta t_{DM}), \quad (15)$$

where

$$\Delta t_{CFL} = \min_i \left(C_{CFL} \frac{r_i - r_{i-1}}{|v_i - v_{i-1}| + \sqrt{\gamma(\gamma - 1)u_i}} \right), \quad (16)$$

and Δt_{DM} is given in equation (10). In the simulations we use $C_{CFL} = 0.25$. The way we couple the two components is by advancing the dark matter particles a timestep Δt_{DM} , and then repeatedly advancing the gas until a further step Δt_g would take the gas ahead of the dark matter. At this point we just take the timestep required to synchronize the two components. The contribution of the dark matter to the total mass M_i inside each gas shell is linearly interpolated in time. We use a force-average scheme similar to equations (6) to (9) to integrate the gas equations, but in this case the final advanced quantities are used to re-evaluate the accelerations at the end of each step before starting the next one. Forces are thus computed twice per time step.

2.3 The cooling

We consider a primordial plasma (i.e. hydrogen and helium only) with a helium mass fraction $Y = 0.24$. The integrations are started at redshift $z_i = 500$, just after recombination. The temperature of the gas is assumed to be uniform and equal to the temperature of the CMB, i.e. $T = 2.726(1 + z_i)$ K (Mather *et al.* 1994). The initial fractional abundances relative to the total number density of hydrogen are taken to be:

$$x_{H^+} = x_e = 1.2 \times 10^{-5} \frac{\Omega_o^{1/2}}{(h\Omega_B)^{-1}}, \quad (17)$$

$$x_{He^+} = x_{He^{++}} = 0. \quad (18)$$

Equation (17) is the fit to the residual ionization fraction of hydrogen by Peebles (1993). Helium would have recombined at an earlier epoch, so we can assume it neutral (Shapiro, Giroux & Babul 1994). In all the simulations presented in this paper we took $h = 0.5$ and $\Omega_o = 1$.

We use the ionization and recombination coefficients, and the cooling and heating rates revised by Abel (private communication). In order to reduce the computational time we interpolate the coefficients and rates out of a table constructed beforehand. One has to bear in mind that there are many physical processes that can affect the emissivity of a hot primordial plasma in a drastic way (e.g. the presence of ionizing radiation, thermal conductivity by electrons, molecular hydrogen formation) and it is beyond the scope of this paper to study all their effects.

We have assumed that electrons and protons have the same temperature. At the shock front it is the ions, and not the electrons, that are initially heated; the electrons are heated later by some mechanism which is at least as fast as Coulomb interactions with the positive ions (Shapiro & Moore 1976). The Coulomb equilibration time is given by

$$t_{e-i} n_H \approx 9.5 \frac{1 - Y}{1 - 0.75Y} \left[\frac{T}{10^5 \text{ K}} \right]^{3/2} \text{ yr cm}^{-3}, \quad (19)$$

(Spitzer 1962), and the cooling time, defined as

$$t_{cool} = \frac{(3/2)nkT_{vir}}{n_H^2 \Lambda(T_{vir})}, \quad (20)$$

can be written more conveniently as

$$t_{cool} n_H \approx \frac{6.6 \times 10^4}{(1 - Y)\mu} \left[\frac{\Lambda(T)}{10^{-23} \text{ erg cm}^{-3} \text{ s}^{-1}} \right]^{-1} \times \left[\frac{T}{10^5 \text{ K}} \right] \text{ yr cm}^{-3}, \quad (22)$$

where μ is the mean molecular weight and Y is the primordial helium fraction by mass. In Figure 1a one can see that the Coulomb equilibration time is smaller than the cooling time up to very high temperatures, of the order of 10^8 K. It is thus a reasonable assumption to adopt a single post-shock temperature for electrons and ions.

Whenever a mostly neutral plasma gets shock-heated up to the virial temperature T_{vir} , the ionization time, $t_{ion} = (n_e \alpha)^{-1}$, can be longer than the cooling time (n_e is the electron number density and α is the collisional ionization rate). The implication is that ionization of the plasma lags behind shock-heating, and line cooling can be enhanced by the higher neutral fractions. As one can see in Figure 1a, this is the case up to temperatures of the order of 10^6 K (i.e. $V_c \sim 160 \text{ km s}^{-1}$). On the other hand, the UV flux radiated

by the hot shocked plasma can preionize hydrogen and helium upstream of the shock provided $V_s > 110 \text{ km s}^{-1}$ (Shull & McKee 1979), where V_s is the shock velocity in the rest frame of the shock. In our systems $V_s \sim 1.2 V_c$, so we expect the plasma to be preionized for halos with $V_c > 100 \text{ km s}^{-1}$. We do not take this effect into account in this paper.

In higher circular velocity halos, the postshock heated gas quickly relaxes to the ionization equilibrium abundances. As the plasma reaches higher densities the cooling time decreases and eventually the gas begins to cool efficiently, while maintaining a higher ionized fraction. The reason is that the recombination time-scales, $t_{rec} = (n_e \beta)^{-1}$, are much longer than the cooling time-scale (β is the recombination rate). In Figure 1b we can see that if the gas gets heated above 10^6 K it will cool out of ionization equilibrium.

Because of the various possibilities, we do not assume equilibrium abundances for the different ions, but rather solve the full rate equations,

$$\frac{1}{x_e} \frac{dx_{\text{H}^+}}{dt} = \frac{1}{\mathcal{C}} \tilde{\rho}_g \{ \beta_{\text{H}^0} x_{\text{H}^0} - \alpha_{\text{H}^+} x_{\text{H}^+} \}, \quad (23)$$

$$\frac{1}{x_e} \frac{dx_{\text{He}^+}}{dt} = \frac{1}{\mathcal{C}} \tilde{\rho}_g \{ \beta_{\text{He}^0} x_{\text{He}^0} + \alpha_{\text{He}^{++}} x_{\text{He}^{++}} - (\beta_{\text{He}^+} + \alpha_{\text{He}^+}) x_{\text{He}^+} \}, \quad (24)$$

$$\frac{1}{x_e} \frac{dx_{\text{He}^{++}}}{dt} = \frac{1}{\mathcal{C}} \tilde{\rho}_g \{ \beta_{\text{He}^+} x_{\text{He}^+} - \alpha_{\text{He}^{++}} x_{\text{He}^{++}} \}, \quad (25)$$

where x_i is the fractional abundance of the species i relative to hydrogen, and β_i (α_i) are the ionization (recombination) rates in units of $\text{cm}^3 \text{ s}^{-1}$. The time \tilde{t} is given in the units,

$$\mathcal{T} = H_o^{-1} = 9.78 h^{-1} \text{ Gyr}, \quad (26)$$

the density $\tilde{\rho}_g$ in the units,

$$\mathcal{D} = \frac{3H_o^2}{4\pi G} = 3.753 \times 10^{-29} h^2 \text{ gr cm}^{-3}, \quad (27)$$

and the factor \mathcal{C} has the units of a reaction rate,

$$\mathcal{C} = 1.429 \times 10^{-13} (1 - Y_P)^{-1} h \text{ cm}^3 \text{ s}^{-1}. \quad (28)$$

Equations (23)-(25) are written under the assumptions that the coronal limit is valid and the total number density of hydrogen varies on a much longer time scale than the ionization state of the plasma. It might happen that the problem is stiff, and then, cannot be handled efficiently by many integration schemes. We use the subroutine LSODAR, coded by L. Petzold and A. Hindmarsh to deal with stiff ordinary differential equations (Hindmarsh 1983).

If cooling/heating terms in the energy equation (equation 13) are treated explicitly, the gas timestep has to be limited as well by the cooling time (equation 20). However, the timestep will become to small whenever strong cooling occurs. To prevent this from happening, the code uses an operator splitting scheme (Press *et al.* 1992). In a real case the microphysical processes operate continuously while the flow is evolving, but there is no way of maintaining this simultaneity without paying a big price in the total computing time. The temperature at the end of a timestep T_i^{n+1} is the solution to the nonlinear algebraic equation,

$$\frac{T_i^{n+1}}{T_{\text{vir}}} = 2(\gamma - 1) \frac{\mu_i^{n+1} (\tilde{\rho}_{g_i}^{n+1}, T_i^{n+1})}{\mu_o} [(\tilde{u}_i^{n+1})_{\text{ad}} + \frac{1}{\mathcal{C}} \tilde{\rho}_{g_i}^{n+1} S(\tilde{\rho}_{g_i}^{n+1}, T_i^{n+1}) \Delta \tilde{t}_g^n], \quad (29)$$

where $(\tilde{u}_i^{n+1})_{\text{ad}}$ and $\tilde{\rho}_{g_i}^{n+1}$ are the specific internal energy and the density which result from integrating the gas dynamics equations without including the radiative terms, μ_o is the mean molecular weight of a fully ionized primordial plasma, and T_{vir} is the virial temperature of the hosting halo,

$$T_{\text{vir}} = 6 \times 10^5 \mu_o \left[\frac{V_c}{100 \text{ km s}^{-1}} \right]^2 \text{ K}. \quad (30)$$

The factor \mathcal{L} ,

$$\mathcal{L} = 2.377 \times 10^{-23} (1 - Y_P)^{-2} h^{-1} \left[\frac{V_c}{100 \text{ km s}^{-1}} \right]^2, \quad (31)$$

and the function $S(\rho_g, T)$,

$$S(\rho_g, T) \equiv \frac{\Gamma(\rho_g, T) - \Lambda(\rho_g, T)}{n_{\text{H}}^2}, \quad (32)$$

are both in units of $\text{erg s}^{-1} \text{ cm}^3$.

The main complication to find a solution to equation (29) is that the ionisation state of the plasma depends on the final temperature. We have designed an iteration scheme to find the temperature and the ionisation state at the end of the timestep. A first guess for the temperature is taken to be $T_i^{(1)} = T_i^n$. The rate equations are integrated, and the obtained fractional abundances are plugged in the right hand side of equation (29) to get a predicted temperature T_i^* . If the error function,

$$\epsilon_i^{(1)} = 1 - \frac{T_i^*}{T_i^{(1)}}, \quad (33)$$

is smaller than 0.001 in absolute value, then $T_i^{n+1} = T_i^*$ and the integration is complete. If this is not the case a second guess for the temperature is taken to be,

$$T_i^{(2)} = \left[1 - 0.1 \text{ sig}(\epsilon_i^{(1)}) \right] T_i^{(1)}, \quad (34)$$

where $\text{sig}(\epsilon_i^{(1)})$ is the signature of the error function. The rate equations are integrated and the whole process is repeated until the error function is smaller than 0.001, or changes sign. In the later case the root to equation (29) is bracketed with a 10% error, and the Van Wijngaarden-Dekker-Brent root finder (Press *et al.* 1992) is used to find T_i^{n+1} with a relative error smaller than 0.1%.

2.4 Inner boundary

Once the gas has been able to cool efficiently it piles up near the centre, and, since the calculations are performed in a Lagrangian frame, the nodes of the grid get extremely concentrated. This causes the code to require very small timesteps. Thoul & Weinberg (1995) got around this problem by freezing at a certain distance r_c those zones for which the cooling time has become much shorter than the dynamical time. However, they found that the amount of cooled mass was sensitive to this central boundary condition, and could vary by $\sim 10\%$ depending on the number of shells used. In addition, a recent numerical study of the stability of radiative shocks indicates that these zones play an important role (Strickland & Blondin 1995). Therefore we keep the innermost zone dynamically active, but we merge overlying zones with it whenever their temperature becomes smaller than a $T_C = 8000 \text{ K}$.

3 TESTS OF NUMERICS

3.1 Adiabatic collapse

Bertschinger (1985) found similarity solutions for secondary infall and accretion onto a seed mass in an Einstein de-Sitter universe. He studied not only collisionless and collisional collapses, but also the collapse of non-self-gravitating gas moving in the potential of a collisionless component. These solutions provide a good testing ground for the dynamics of our code in the absence of the cooling processes. In WZ's model, Bertschinger's solutions correspond to $\epsilon = 1$ and no angular momentum (i. e. $e = 1$). However, in order to avoid integration problems near the centre we prefer to use slightly non-radial orbits for the dark matter with an eccentricity $e = 0.9$.

The self-similarity arises from the fact that there are no preferred scales in the initial perturbation, and therefore, the whole evolution of the system is determined only by the rate at which matter turns around. Following Bertschinger we nondimensionalize variables as follows:

$$r = r_t \lambda \quad (35)$$

$$v(r, t) = \frac{r_t}{t} V(\lambda) \quad (36)$$

$$\rho(r, t) = \rho_H D(\lambda) \quad (37)$$

$$P(r, t) = \rho_H \left(\frac{r_t}{t} \right)^2 P(\lambda) \quad (38)$$

$$m(r, t) = \frac{4}{3} \pi \rho_H r_t^3 M(\lambda) \quad (39)$$

where ρ_H and r_t are the mean cosmic density and the turn-around radius at time t .

We first performed a calculation assuming a collisionless component and using 15000 shells. This simulation settled down to self-similar evolution which reproduced Bertschinger's solution almost perfectly except for small differences in the inner regions resulting from the fact that our shells have slightly nonradial orbits. The total energy was conserved up to 0.3%. We also calculated a collisionless collapse with $\epsilon = 2/3$ and $e = 0.7$. Our numerical solution agrees well with that given by White & Zaritsky (1992). The mass profile at redshift z is linear in radius out to,

$$r_{\text{vir}} \approx 120 (1+z)^{-3/2} h^{-1} \left[\frac{V_c}{100 \text{ km s}^{-1}} \right] \text{ kpc}, \quad (40)$$

and contains a mass,

$$M_{\text{vir}} \approx 2.8 \times 10^{11} (1+z)^{-3/2} h^{-1} \left[\frac{V_c}{100 \text{ km s}^{-1}} \right]^3 M_{\odot}. \quad (41)$$

The self-similar solution for a collisional gas is obtained using a grid with 500 particles. We have simulated only the adiabatic case $\gamma = 5/3$, and find very good agreement with Bertschinger's similarity solution (see Table 1). The TAV scheme we have adopted proved to be very efficient in producing a sharp shock profile with practically no post-shock oscillations. We have also calculated a collisional collapse with both gas and a gravitationally dominant collisionless component ($\Omega_B = 0.05$). In this case the agreement with Bertschinger's solution is also good (see Table 2), but we observe some post-shock oscillations, especially in the velocity profile. This is a spurious effect due to discrete jumps in the gravitational forces which occur whenever a dark matter shell crosses a gas zone. To reduce such effects we have to

make sure that the shell masses are small enough compared to the gas zone masses. For equal masses this condition can be written as,

$$\frac{N_{DM}}{N_g} \geq \frac{\Omega_{DM}}{\Omega_g}, \quad (42)$$

where N_{DM} , N_g are the number of dark matter shells and gas zones respectively (Thoul & Weinberg 1995). The total energy was conserved up to 0.2%.

3.2 Radiative processes

In order to test our radiative processes subroutine we have calculated the thermal evolution of the intergalactic medium (IGM) in the absence of any perturbation. We assume, following Miralda-Escudé & Rees (1994), that the IGM was fully ionized at a redshift z_{in} , and heated up to a temperature T_{in} . In their calculations these authors took $\Omega_B = 0.05$, and we have also studied the cases $\Omega_b = 0.01$, 0.025 and 0.1. In the first case we find a good agreement with the published results. For a lower Ω_B the final temperature of the IGM turns out to be lower, while for a higher baryonic content the final temperature is higher. This is the expected behaviour since the recombination rates decrease with density, and consequently photoionization is not so effective at heating the gas.

We have also studied the thermal evolution of an overdense region, for which the density is given by the top-hat model until virialization, and is assumed constant thereafter. Once again the agreement with Miralda-Escudé & Rees (1994) is good. Now the final temperature of the cloud decreases as we increase the baryonic content of the Universe. This is because at higher densities photoionization is not effective anymore and the dominant process is line cooling, which has an emissivity that increases with density.

4 COLLAPSE SIMULATIONS

4.1 Nonradiative collapse

First of all we obtain the similarity solutions that arise from a power-law initial perturbation with index $\epsilon = 2/3$ in the absence of radiative cooling. If variables are scaled as in equations (35)-(39) the partial differential equations which describe the gas hydrodynamics transform into a set of ordinary differential equations,

$$(V - \lambda)D' + DV' + \frac{2}{\lambda}DV - 2D = 0, \quad (43)$$

$$(V - \lambda)V' = -\frac{P'}{D} - \frac{2M}{9\lambda^2}, \quad (44)$$

$$(V - \lambda) \left(\frac{P'}{P} - \gamma \frac{D'}{D} \right) = 2(1 - \gamma), \quad (45)$$

$$M' = 3\lambda^2 D, \quad (46)$$

where primes denote derivatives with respect to λ .

Far away from the origin the solution for cold accretion applies, in which case analytic expressions can be obtained (for details see Forcada-Miró 1997),

$$\lambda = \sin^2 \left(\frac{\theta}{2} \right) \frac{\pi}{\theta - \sin \theta}, \quad (47)$$

$$V = \frac{\pi}{2} \cot\left(\frac{\theta}{2}\right), \quad (48)$$

$$M = \left(\frac{3\pi}{4}\right)^2 \frac{\pi}{\theta - \sin\theta}, \quad (49)$$

$$D = \frac{1}{3} \left(\frac{3\pi}{4}\right)^2 \frac{\sin^{-2}\left(\frac{\theta}{2}\right)}{\lambda(\lambda - V)}, \quad (50)$$

where $\theta \in [0, 2\pi]$. Turnaround corresponds to a value of the parameter $\theta_t = \pi$.

At a given $\lambda = \lambda_s$ the nondimensional strong shock jump conditions,

$$V_2 - \lambda_s = \left(\frac{\gamma - 1}{\gamma + 1}\right) (V_1 - \lambda_s), \quad (51)$$

$$D_2 = \left(\frac{\gamma + 1}{\gamma - 1}\right) D_1 \quad (52)$$

$$P_2 = \frac{2}{\gamma + 1} D_1 (V_1 - \lambda_s)^2, \quad (53)$$

$$M_2 = M_1, \quad (54)$$

provide the postshock values from which the ordinary differential equations (43)-(46) are solved using a Runge-Kutta integrator (Press *et al.* 1992). The solution obtained for $\gamma = 5/3$ is plotted in Figure 2. There is only one position of the shock $\lambda_s^o \approx 0.29$ for which the boundary condition $V(0) = M(0) = 0$ is satisfied. In this case the solution has an asymptotic behaviour near the origin,

$$D \sim \lambda^{-2}, \quad P \sim \lambda^{-2}, \quad M \sim \lambda. \quad (55)$$

The density profile is due to the fact that shells settle at a constant fraction of their turnaround radius. The pressure profile is a consequence of pressure forces balancing gravity in the static regions. If the shock is at a smaller λ_s then gravity rapidly dominates over pressure gradients and the fluid approaches adiabatic free-fall as it flows inwards:

$$V \sim \lambda^{-1/2}, \quad D \sim \lambda^{-3/2}, \quad P \sim D^\gamma. \quad (56)$$

Each fluid particle crosses the origin at a finite time, and thus, there is a mass flux through the inner boundary; in the limit $\lambda_s = 0$ the solution for cold accretion is recovered. On the other hand, if $\lambda_s > \lambda_s^o$ the mass goes to zero and the density diverges at a position $0 < \lambda_o < \lambda_s$. Notice that only the solution with $\lambda_s = \lambda_s^o$ is physical.

The introduction of a dominant collisionless component does not change the solution significantly from the purely gaseous case. We have performed the calculations for a baryonic content $\Omega_B = 0.05$ and eccentricities $e = 0.9, 0.7, 0.5$. In the self-gravitating case the shock position is only of the order of 1% smaller, and thus, the evolution in redshift of r_s is well approximated for any baryonic content $\Omega_B \in [0, 1]$ by the expression,

$$r_s \approx 130 (1+z)^{-3/2} h^{-1} \left[\frac{V_c}{100 \text{ km s}^{-1}} \right] \text{ kpc}, \quad (57)$$

and the gas mass within,

$$M_s \approx 3 \times 10^{11} (1+z)^{-3/2} \Omega_B h^{-1} \left[\frac{V_c}{100 \text{ km s}^{-1}} \right]^3 M_\odot. \quad (58)$$

The mean overdensity enclosed by the shock is then $\bar{D}_s \approx 120$, smaller than the usually assumed value of 200 (White & Frenk 1991). It is also interesting that the infalling gas hits

the shock with a velocity very close to the circular velocity of the inner halo.

4.2 Radiative collapse

The similarity solutions of the last section assume no radiative cooling. However, if the virial temperature of the system is above the sharp cut-off of the cooling curve at approximately $10^4 K$ the post-shock gas will be able to radiate, and the evolution of the system will be modified. According to equation (29) cooling should be important in halos with a circular velocity $V_c \geq 17 \text{ km s}^{-1}$. We have calculated the time evolution of systems with circular velocity 20, 40, 60, 80, 100, 140, 180, 220 and 300 km s^{-1} , and with gas fractions, $\Omega_B = 0.05$ and 0.1 . Throughout this paper we adopt $H_o = 50 \text{ km s}^{-1} \text{ Mpc}^{-1}$.

Radiative cooling introduces a new scale length into the problem, the cooling radius, defined as the radius at which the cooling time equals the lifetime of the system. The self-similarity we had in the nonradiative collapses is therefore broken. At a given epoch, the cooling radius and the shock radius are at different fractions of the turnaround radius for each circular velocity. For a given circular velocity these fractions change with time (see 4.2.1 and 4.2.2).

The details of the behaviour of the radiative shock depend on whether the hosting halo has a circular velocity above or below 100 km s^{-1} . We therefore separate discussion of these two cases in the next two subsections. In the high circular velocity case the virial temperature is bigger than $3 \times 10^5 \text{ K}$ and thermal bremsstrahlung dominates the cooling. Line emission by H and He^+ provide the cooling processes in smaller halos.

4.2.1 High circular velocity halos

In Figure 3 we show the evolution of the radial structure of a halo like that of the Milky Way, i.e. $V_c = 220 \text{ km s}^{-1}$. The variables in this figure have been scaled as in equations (34-38); Θ is the temperature scaled to the virial temperature of the system (equation 29). For this example we have chosen $\Omega_b = 0.05$.

At early times, the density profile inside the shock is well fitted by a power-law exponent -1.5 , the expected solution for a cooling flow in an isothermal potential well (Bertschinger 1989). At later times, the profile has the exponent of the nonradiative model, -2 , from the shock radius down to the cooling radius, and then at smaller radii it bends to an exponent of -1.5 . The pressure profile is always slightly steeper than the density profile, because residual departures from hydrostatic equilibrium and the transition from the noncooling to the cooling regime all cause the temperature to increase inwards. At early times, the exponent for the pressure profile is roughly -1.8 over the regions we resolve, while at later times it is roughly -2.3 from the shock to the cooling radius, bending to -1.8 at smaller radii. The mass profiles follows in the outer regions the adiabatic collapse solution, and in the inner regions is dominated by the mass M_{cool} that has cooled below 8000 K . At early times M_{cool} is close to the mass of the black hole in the case of cold accretion, and decreases as the system evolves in time.

As gas passes through the cooling radius, radiative effects become important; nevertheless, its temperature and

density increase continually until its cooling time becomes shorter than the local dynamical time and catastrophic cooling takes place. The reason is that as the gas radiates and flows inwards, compressional heating dominates over radiative cooling. At the point where catastrophic cooling takes place, the material gets very cold and dense and piles up near the center. We cut our plots at this point because our code cannot resolve the structure of the cold central region.

Another consequence of this inflow is that the gas is more centrally concentrated than the dark matter, which in principle could be a possible way of explaining the larger baryon fractions measured in rich galaxy clusters (Babul & Katz 1993). If we plot the baryon enhancement at a given time for different halos we see that the bigger the halo the closer we are to the adiabatic solution (Figure 4). On the other hand, for each individual halo the global expansion of the Universe reduces all densities and so makes radiative cooling progressively less efficient with time. As a result the gas enhancement gets weaker as the system evolves. This explains why the profile of enclosed gas mass in Figure 3 gets steeper with time. However, White *et al.* (1993) proved that even assuming the most extreme case of cold accretion one cannot account for the observed baryon fractions in clusters of galaxies. Cooling processes alone cannot therefore enhance the cluster baryon fraction in an Einstein-de Sitter Universe to the values required for consistency with Ω_B as inferred from Big Bang nucleosynthesis.

In Figure 5 we present the evolution of the shock radius and the cooling radius for circular velocities 140, 180, 220 and 300 km s⁻¹, and in Figure 6 the evolution of the mass within these radii. In these simulations the central resolution is such that the shock forms at a redshift $z \sim 50$. At early times all the gas that goes through the shock is able to radiate away most of its internal energy. As a result, the shock wave and the cooling wave move together, their position increasing approximately as $\sim t^\alpha$, with α decreasing slightly with circular velocity. At later times the cooling wave separates from the shock wave, because the post-shock density is no longer high enough for rapid cooling, and the shock position and the mass it contains grow in time in proportion to $t^{1/2}$, as in Bertschinger’s (1986) similarity solution. The shock wave asymptotically approaches the nonradiative regime, its position and mass growing linearly in time. Figure 6 also shows the total mass that has cooled below 8000 K, and so is included in the central zone.

4.2.2 Low circular velocity halos

The behaviour of the radiative shocks in systems with $V_c < 100$ km s⁻¹ differs significantly from that in higher circular velocity halos. In order to clarify the situation in this case we have followed the evolution over longer timescales, corresponding to epochs beyond $z = 0$. In order to do this it was necessary to reduce the central resolution slightly; the shock then forms at a redshift $z \sim 25$.

The most noticeable feature of these simulations is that the shock front is unstable to large amplitude oscillations when $20 \text{ km s}^{-1} < V_c < 80 \text{ km s}^{-1}$ (Figure 7). The onset of these oscillations takes place earlier with decreasing circular velocity. Their amplitude and period grow as the system gets older, and, in the cases with 40 and 60 km s⁻¹, they die out at later times. The oscillations can also be seen in plots of

the mass within the cooling and shock radii (Figure 8). It is interesting that during most of the oscillatory evolution no gas cools below 8000 K; only at the very end of the cycle does strong cooling allow a burst of mass accretion onto the central object.

Radiative shocks have been found to be unstable to oscillations in other astrophysical contexts. Langer, Chamugam & Shaviv (1982) simulated time-dependent accretion onto white dwarfs and found that the cooling layer suffers oscillatory instabilities if the rate of accretion is above a certain critical value. Improved hydrodynamical simulations showed that these radiative shocks are unstable to oscillations if the cooling rate $\Lambda \sim \rho^2 T^c$ has a dependence on temperature such as $\alpha < 0.6$, in quite good agreement with linear stability analysis (Imamura, Wolf & Durisen 1984).

These studies considered equilibrium ion abundances, and in our calculation we use time-dependent cooling. Therefore, our cooling function is dependent on the history of the plasma. Gaetz, Edgar & Chevalier (1986) addressed the question of stability of radiative shocks with time-dependent cooling and concluded that, although a precise stability limit cannot be established, simple power-law approximations of the cooling curve give a rough idea of the driving physics.

With a power-law approximation the cooling function, the cooling time of a gas element goes as,

$$t_{\text{cool}} \sim \rho_g^{-1} T^{1-c}. \quad (59)$$

The post-shock temperature T_s of the gas is related to the pre-shock infall velocity v_1 and the shock velocity v_s through the strong shock jump conditions:

$$T_s \sim (v_1 - v_s)^2. \quad (60)$$

If the shock moves outwards the gas is heated to a higher temperature, while the post-shock density drops (Figure 9). This leads to an increased cooling time, particularly for small c , and so to increased pressure in the region behind the shock. This excess pressure drives the shock further outwards in a very short timescale. In this expansion phase the density, temperature and pressure profiles are rather featureless, with slopes close to the cooling regime discussed in Section 4.2.1 (Figure 10).

Eventually, the density of the downstream gas increases to the point where cooling again becomes substantial; pressure support for the shock then weakens and the shock slows down. The gas is now heated to a smaller temperature and can cool more efficiently (Figure 9). As a result of this cooling instability a density peak forms behind the shock (Figure 10). The rapid cooling of the gas in the density peak produces a further loss of pressure support and the shock falls in with the flow. It is during this final collapse that cold gas is accreted onto the centre during a relatively short ‘‘burst’’. A pressure build-up near the centre eventually causes the infalling shock to strengthen again and to reverse its motion. As a result of the cosmic expansion, it takes longer for the post-shock gas to cool in each new cycle, causing the period and amplitude of the oscillations to increase.

In our models we see such oscillatory behaviour when $V_c \leq 80 \text{ km s}^{-1}$. This suggests that the critical slope of the cooling function for instability is $c \sim 0$. For the primordial element abundances which we assume, c is reduced below the value $c = 0.5$ expected for bremsstrahlung as he-

lium line cooling enhances the radiation at lower temperatures. Including heavier elements in our cooling function would cause the transition to oscillatory behaviour to move to higher V_c .

Another interesting result is that in these low circular velocity halos the gas component is more concentrated for a given fraction of the turnaround radius than in bigger systems (Figure 4). However, observations of dwarf galaxies seem to indicate that they are dark-matter dominated (Kormendy 1988). Therefore, one needs some physical mechanism to dilute the baryon component in the smaller systems if one wants to reconcile this theory of galaxy formation with observations. Dekel & Silk (1986) roughly estimated that a starburst could cause loss of most of the gas in a halo with circular velocity below a critical value of the order of 100 km s^{-1} . Their proposed mechanism is supernova-driven winds, since gas absorbs radiation emitted by young stars very inefficiently. It is quite uncertain how much mass is lost by this mechanism which must be effective well before most of the gas turns into stars.

5 THEORETICAL MODEL

We desire to present physical explanations for the evolution in time of the shock and cooling wave. In order to accomplish this, we have used as a starting point the ideas set out in White & Frenk (1991). They pointed out that due to the general expansion of the Universe the shock will go through two very distinct epochs:

(i) Infall-dominated phase: Initially the density is high enough that all the gas that gets shock-heated is able to cool (i.e. $t_{\text{cool}} < t$, where t is the lifetime of the system). At this time the supply of cold gas is limited by the infall rate rather than by cooling.

(ii) Cooling-dominated phase: After a certain time the density becomes too low and the post-shock gas cannot cool efficiently anymore (i.e. $t_{\text{cool}} > t$). At this stage the amount of cold gas is regulated by radiative losses.

These two epochs have been clearly seen in the numerical simulations presented in Section 4, and we will study them now in more detail.

5.1 Infall-dominated regime

During the infall-dominated phase the gas is able to cool so efficiently that it rapidly loses pressure support. Consequently it flows towards the centre, most of the cooling layer being covered while the matter is still travelling at the post-shock velocity. The thickness of the cooling layer is then roughly,

$$\Delta r_{\text{cool}} \sim v_s t_{\text{cool}}. \quad (61)$$

As the gas cools it is compressed to high density. The whole process can be regarded as an isothermal shock, and thus the compression factor is,

$$\rho_2 \approx \mathcal{M}_s^2 \rho_1 \quad (62)$$

where \mathcal{M}_s is the Mach number of the shock,

$$\mathcal{M}_s \approx \left(\frac{\mu m_p v_s^2}{\gamma k_B T_c} \right)^{1/2} \gg 1. \quad (63)$$

and T_c is the gas temperature, which is of the order of the cut-off temperature in the cooling curve (i.e. $T_c \sim 10^4 \text{ K}$). The thickness of the cold layer can be roughly estimated from mass conservation,

$$\Delta r_{\text{cold}} \approx \mathcal{M}_s^{-2/3} r_s. \quad (64)$$

Therefore, the shock will be at a position,

$$r_s \approx \Delta r_{\text{cool}} \gg \Delta r_{\text{cold}}, \quad (65)$$

which implies that the shock moves in the quasi-equilibrium,

$$t_{\text{cool}} \sim t_{\text{ff}}, \quad (66)$$

where t_{ff} is the freefall timescale,

$$t_{\text{ff}} = \frac{1}{\sqrt{24\pi G \bar{\rho}}} \sim \left(\frac{M_s}{\lambda_s^3} \right)^{-1/2} (1+z)^{-3/2}, \quad (67)$$

and $\bar{\rho}$ is the mean density of total mass within a given radius. If the cooling time is bigger than the free-fall time adiabatic heating will increase the temperature of the gas thereby reducing the cooling time. In the opposite situation the temperature rapidly decreases, and thus, the cooling time increases.

At very early times Compton scattering provides the dominant source of energy loss (Silk 1977). In this case, the cooling time depends only on the redshift,

$$t_{\text{comp}} \approx 2.4 \times 10^{12} (1+z)^{-4} \text{ yr}. \quad (68)$$

According to equation (66), the evolution of the shock is qualitatively given by,

$$\frac{M_s}{\lambda_s^3} \sim (1+z)^5. \quad (69)$$

The gas flows inwards until it becomes self-gravitating, which implies that M_s is roughly a constant,

$$M_s \approx \Omega_B M_o, \quad (70)$$

where M_o is the nondimensional mass ***what does this mean?*** of the black hole in the cold collapse solution. Therefore, the position of the shock evolves in time as,

$$r_s \sim \Omega_B^{1/3} t^{19/9}. \quad (71)$$

The rate of energy loss due to Compton scattering decreases with a high power of the redshift, and eventually two-body processes will dominate the radiative cooling of the system. In this case the cooling time depends on the nondimensional hydrodynamic variables as,

$$t_{\text{cool}} \sim D_1^{-1} V_1^{2(1-c)} (1+z)^{-3}, \quad (72)$$

and the qualitative evolution of the radiative shock is given by,

$$\Psi(\lambda; c, \Omega_B) \equiv D_1 V_1^{-2(1-c)} \left(\frac{M_s}{\lambda_s^3} \right)^{-1/2} \sim (1+z)^{-3/2}, \quad (73)$$

where the function $\Psi(\lambda; c, \Omega_B)$ depends on two parameters: the slope of the cooling function c , and the baryonic content of the universe Ω_B . For a self-gravitating gas one has the asymptotic behaviour,

$$\Psi(\lambda \ll 1; c, \Omega_B) \approx \Psi_o(\Omega_B) \lambda^{1-c}, \quad (74)$$

where $\Psi_o(\Omega_B)$ increases as the baryonic fraction decreases, and diverges for $\Omega_B \rightarrow 0$. Therefore, the physical position of the radiative shock has a power-law behaviour in time,

$$r_s(t; c, \Omega_B) \approx r_o(\Omega_B) t^{\frac{2-c}{1-c}}, \quad (75)$$

where $r_o(\Omega_B)$ decreases with the baryonic fraction, and $r_o(\Omega_B) \rightarrow 0$ as $\Omega_B \rightarrow 0$.

The radius of the shock wave in the infall-dominated regime grows faster than linearly in time; as a result the nondimensional shock position λ_s increases as the system evolves. The slope of the function $\Psi(\lambda; c, \Omega_B)$ increases with λ , and thus, the power-law behaviour of r_s decreases approaching a linear growth in time (Figure 11). Eventually, the postshock cooling time becomes bigger than the lifetime of the system, and the shock enters the cooling-dominated regime. An upper limit to the position at which this transition happens is provided by the nonradiative shock (i.e. $\lambda_s \approx 0.29$). At this point, r_s has roughly a power-law behaviour,

$$\alpha \approx \frac{1.5 - c}{1 - c}. \quad (76)$$

Therefore, if one fits a single power-law to the time evolution of the radiative shock one should obtain a value in between these two limits.

One has to keep in mind that the softened gravity prevents the collapse beyond the resolution limit of the code, and the shock forms at a position close to the softening parameter a . For $r < a$ a cold dense core forms, where the density is constant in radius and the material is at rest. At this stage the shock strongly violates the quasi-equilibrium condition, with $t_{\text{cool}} \ll t_{\text{ff}}$. In the numerical simulations which do not present an oscillatory instability we have fitted an analytical expression of the form $r_s = a + bt^\alpha$ to the evolution in time of the shock radius (Figure 5 and Figure 7). The fitted exponent is in all cases between the predicted limits, and for the high velocity halos is fairly constant, with a value close to $\alpha = 2$. This is the exponent expected when Compton cooling is still a significant source of cooling (Figure 12).

5.2 Cooling-dominated regime

The transition to the cooling-dominated regime happens when the postshock cooling time equals the lifetime of the system. According to equations (66) and (69) the mean total overdensity has a well defined value at this time. This is in agreement with the fact that in the simulations the nondimensional position at which the shock transits is the same for all halos with a very small scatter (Table 3). Also the postshock temperature is very close to the virial temperature of the system.

The nondimensional position of the shock at the time of transition is very close to the case $\gamma = 4/3$. In fact, radiative cooling weakens the pressure support of the gas against gravity, making the equations of state less stiff; in other words, radiative cooling leads to an effective ratio of specific heats $\gamma_{\text{eff}} < 5/3$, and, if the gas cools strongly, even $\gamma_{\text{eff}} < 4/3$. The numerical simulations suggest that one can think of the evolution in time of a collapsing halo as ‘‘passing’’ through a series of adiabats. At early times, when radiative cooling is very strong, one has $\gamma_{\text{eff}} < 4/3$. This exponent increases with time towards $\gamma = 5/3$. The value $\gamma = 4/3$ delimits

the boundary between the infall-dominated and the cooling-dominated regime.

With the appropriate choice of temperature and gas density one can obtain a fairly good estimate of the redshift z_{cf} at which the cooling-dominated phase starts. If one takes a temperature equal to the virial temperature of the halo, and a density equal to the mean gas overdensity inside the nonradiative shock the predictions compare well with the results from the simulations (Figure 13). Now, for a given halo, the physical size at the time the transition takes place is simply,

$$R_{\text{cf}} \approx 10 \left[\frac{1 + z_{\text{cf}}}{1 + z_{\text{cf}}^*} \right]^{-3/2} h^{-1} \left[\frac{V_c}{100 \text{ km s}^{-1}} \right] \text{ kpc}, \quad (77)$$

where $z_{\text{cf}}^* = 3$ is a characteristic redshift, and the total mass of cold gas enclosed in solar masses is,

$$M_{\text{cf}} \approx 3.8 \times 10^{10} \left[\frac{1 + z_{\text{cf}}}{1 + z_{\text{cf}}^*} \right]^{-3/2} \Omega_B h^{-1} \left[\frac{V_c}{100 \text{ km s}^{-1}} \right]^3. \quad (78)$$

The simulations show that as soon as the shock enters the cooling-dominated regime a hot halo starts building with an isothermal density profile. The temperature has a slight increase inwards (Figure 3), but we will assume it is a constant and equal to the virial temperature of the hosting halo. At any given time there is a radius $r_c \leq r_s$ at which the gas density is high enough so the cooling time equals the lifetime of the system,

$$t \approx t_{\text{cool}}(r_s) \frac{\rho_g(r_s)}{\rho_g(r_c)}, \quad (79)$$

and since the halo is isothermal,

$$r_c(t) \approx r_s(t) \left[\frac{t}{t_{\text{cool}}(r_s)} \right]^{1/2}. \quad (80)$$

Once the shock has entered the cooling-dominated regime, it gradually approaches the nonradiative behaviour and grows linearly in time. At this stage the postshock cooling time grows proportional to t^2 , and then,

$$r_c(t) \approx r_s(t_o) \left[\frac{t}{t_{\text{cool}}^*} \right]^{1/2}, \quad (81)$$

where t_o is a reference epoch at which the shock presents the nonradiative behaviour, and t_{cool}^* is the post-shock cooling time at the reference epoch.

The cooling time t_{cool}^* is related to the estimated time at which the shock enters the cooling dominated regime t_{cf} as,

$$\frac{t_{\text{cool}}^*}{t_{\text{cf}}} = \frac{\bar{D}_s}{D_s} \left[\frac{t_o}{t_{\text{cf}}} \right]^2, \quad (82)$$

where \bar{D}_s is the mean gas overdensity inside the nonradiative shock and $D_s \approx 27$ is the self-similar postshock density. Combining equations (81) and (82) we have obtained the following analytic approximation for the evolution in time of the position of the cooling wave,

$$r_c(t) \approx \left[\frac{D_s}{\bar{D}_s} \right]^{1/2} r_s(t_{\text{cf}}) \left[\frac{t}{t_{\text{cf}}} \right]^{1/2} \approx \frac{1}{2} r_s(t_{\text{cf}}) \left[\frac{t}{t_{\text{cf}}} \right]^{1/2}. \quad (83)$$

In Figure 5 and Figure 7 one can see that the analytical expression given in equation (83) is a rather good approximation to the position of the cooling wave once the shock

wave presents the nonradiative behaviour. Until this happens the postshock density decreases in time faster than in the self-similar nonradiative evolution, so the cooling radius will be at a smaller fraction of the shock radius than predicted by a power-law scaling. In fact, in Figure 5 one can see that in the early stages of the cooling flow the radius r_c decreases with time. On the other hand, the cooling radius cannot move inwards faster than the flow, so it might happen that the cooling wave is stationary at the early stages, with no mass accretion. The numerical code only gives the position of the cooling radius whenever a cell can first cool efficiently, and thus, a stationary cooling wave will produce a “gap” in the data. This “gap” is clearly seen for $V_c = 300$ km s⁻¹ in both the radius (Figure 5) and the mass evolution (Figure 6), and barely for $V_c = 220$ km s⁻¹. This effect is stronger with increasing circular velocity because the power-law α is bigger (Figure 12).

In the self-similar solutions of Bertschinger (1989) the mass accretion rate at the cooling radius is approximately,

$$\dot{M}_c \approx 4 \pi r_c^2 \rho_g(r_c) \dot{r}_c. \quad (84)$$

so we model the rate at which cold gas accumulates by this simple inflow equation. Since the halo is isothermal down to the cooling radius,

$$r_c^2 \rho_g(r_c) = r_s^2 \rho_g(r_s), \quad (85)$$

and at later times, when the system is well into the cooling-dominated regime, the total mass accreted by the shock is,

$$M_s \approx 4 \pi r_s^3 \rho_g(r_s). \quad (86)$$

Now we can write equation (84) as,

$$\dot{M}_c \approx \frac{M_s}{r_s} \dot{r}_c. \quad (87)$$

According to equation (87), and since the shock evolves like in the nonradiative case, the mass inside the cooling radius grows in time proportional to $t^{1/2}$. In Figure 6 and Figure 8 one can see that a simple power-law scaling,

$$M_c(t) \approx M_s(t_{cf}) \left[\frac{t}{t_{cf}} \right]^{1/2}, \quad (88)$$

is a good approximation for the mass within the cooling radius.

6 CONCLUSIONS

1-D simulations like the ones we have done are a powerful tool to enhance our understanding of the physics involved in the process of galaxy formation. In particular, we have concentrated on the shocks that appear in the collapse of a protogalaxy, and they have been proved to present the features already known from previous studies of strongly radiative shocks in other contexts. The shocks are subject to an oscillatory instability whenever line cooling dominates the radiative losses behind the shock front. Due to the expanding background in which the system is embedded, the period and the amplitude of the oscillations increase with time.

We believe that we now fully understand the effects of radiative cooling in the shocks that appear in spherical models for galaxy formation. Despite the rather complicated

physical behaviour of the shocks, we have been able to build a simple model which explains very well the kinematics both of the shock wave and of the cooling wave in all cases which are not unstable. At early times the shock front evolves in such a way that the cooling time is of the order of the free-fall time. In the bigger halos Compton cooling dominates, and the radius of the shock grows proportional to t^2 . In smaller halos the slope is a function of the slope of the cooling function at the virial temperature of the system. The transition to the cooling-dominated regime happens at the same nondimensional position in all halos. This is close to the position of a nonradiative shock with a ratio of specific heats $\gamma = 4/3$. The time at which each system becomes nonradiative is well estimated assuming a temperature equal to the virial temperature of the system, and an overdensity equal to the mean overdensity inside the nonradiative shock.

Whenever oscillations appear, our model provides only a rough guide to the behaviour. However, one should keep in mind that there are important processes that we have not taken into account, and that affect systems with circular velocities precisely in the range where the shock wave oscillates. The cold dense gas that accumulates in the central regions will form stars, which will provide a flux of ionizing radiation. In addition we should consider a metagalactic background of UV radiation due to high redshift quasars. The effect of such radiation is to maintain a higher ionization fraction which reduces the line cooling. We may expect the oscillatory behaviour to be absent in this case, and lower circular velocity dwarf galaxies be prevented from forming (Efstathiou 1992). We will consider such effects further in a future paper. They have convinced us that further analysis of the oscillatory solutions is unlikely to be worthwhile.

ACKNOWLEDGMENT

M.I. Forcada I Miró would like to thank the Fundación Rich and the Max-Planck Gesellschaft for the economical support. He is thankful as well to Amancio Friaça, Zoltan Haimann, Thomas Plewa and Martin Rees for many helpful discussions.

REFERENCES

- Anninos, W.Y., Norman, M.L., 1994, ApJ, 429, 434 1985, ApJSS, 58, 39
- Babul, A., Katz, N., 1993, ApJ, 406, L51
- Benz W., 1991, Late stages of stellar evolution. Computational methods in astrophysical hydrodynamics, Lecture Notes in Physics 373, ed. C.B. de Loore, Springer, Berlin
- Bertschinger E., 1985, ApJSS, 58, 39
- Bertschinger E., 1989, ApJ, 318, 66
- Binney J., 1977, ApJ, 215, 483
- Blumenthal G.R., Faber S.M., Primack J.R., Rees M.J., 1984, Nature, 311, 517
- Casertano S., van Gorkom J.H., 1991, AJ, 101, 1231
- Cen R., 1992, ApJSS, 78, 341
- Cole S., Aragón-Salamanca A., Frenk C.S., Navarro J.F., Zepf S.E., 1994, MNRAS, 271, 781
- Davis M., Efstathiou G., Frenk C.S., White S.D.M., 1985, ApJ, 292, 371
- Dekel A., Silk J., 1986, ApJ, 303, 39
- Efstathiou, G., 1992, MNRAS, 256, 43P
- Fillmore J.A., Goldreich P., 1984, ApJ, 281, 1
- Forcada-Miró M.I., 1997, Ph.D. Thesis, University of Cambridge
- Gaetz T.J., Edgar R.J., Chevalier R.A., 1988, ApJ, 329, 927
- Gott III J.R., 1975, ApJ, 201, 296
- Gunn J.E., 1977, ApJ, 218, 592
- Haiman, Z., Thoul, A.A., Loeb, A., 1996, ApJ, 464, 523
- Hindmarsh A.C., 1983, Scientific Computing, R.S. Stepleman et al. eds. North-Holland, Amsterdam
- Imamura J.N., Wolff M.T., Durisen R.H., 1984, ApJ, 276, 667
- Katz N., Hernquist L., Weinberg D.H., 1992, ApJ, 399, L109
- Kauffmann G., White S.D.M., Guiderdoni B., 1993, MNRAS, 264, 201
- Kauffmann G., Nusser, A., Steinmetz, M., 1997, MNRAS, 286, 795
- Kormendy J., 1988, in Origin, Structure, and Evolution of Galaxies, Fang, L. Z. ed. , World Scientific Publishing, Singapore, p. 252
- Langer S.H., Chanmugam G., Shaviv G., 1982, ApJ, 258, 289
- Larson D., 1974, MNRAS, 166, 585
- Mather, J.C. et al., 1994, ApJ, 420, 439
- Miralda-Escudé J., Rees M.J., 1994, MNRAS, 266, 343
- Navarro J.F., White S.D.M., 1993, MNRAS, 265, 271
- Ostriker J.P., 1993, ARA&A, 31, 689
- Ostriker J.P., Steinhardt P.J., 1995, Nature, 377, 600
- Peebles P.J.E., 1967, ApJ, 147, 859
- Peebles P.J.E., 1993, Principles of Physical Cosmology, Princeton, Princeton University Press
- Press W.H., Teukolsky S.A., Vetterling W.T., Flannery B.P., 1992, Numerical Recipes in Fortran, Cambridge, Cambridge University Press
- Rees M.J., Ostriker J.P., MNRAS, 179, 541
- Shapiro P.R., Giroux, M.L., Babul, A., 1994, ApJ, 427, 25
- Shapiro P.R., Moore, R.T., 1976, ApJ, 207, 460
- Shapiro P.R., Struck-Marcell C., 1984, ApJSS, 57, 205
- Shull J.M., McKee C.F., 1979, ApJ, 227, 131
- Silk J., 1977, ApJ, 211, 638
- Spitzer L., 1962, Physics of Fully Ionized Gases, 2nd. ed. New York, Interscience
- Steinmetz M., 1996, MNRAS, 278, 1005
- Strickland R., Blondin J.M., 1995, ApJ, 449, 727
- Thoul A.A., Weinberg D.H., 1995, ApJ, 442, 480
- Thoul A.A., Weinberg D.H., 1996, ApJ, 465, 608
- Tscharnutter W.M., Winkler K.H., 1979, CompPhysComm, 18, 171
- White M., Scott D., Silk J., 1994, ARA&A, 32, 319
- White S.D.M., Frenk C.S., 1991, ApJ, 379, 52
- White, S.D.M., Rees, M.J., 1978, MNRAS, 183, 341
- White S.D.M., Navarro J.F., Evrard A.E., Frenk C.S., Nature, 366, 429
- White S.D.M., Zaritsky D., ApJ, 394, 1
- Zaritsky D., White S.D.M., 1994, ApJ, 435, 599

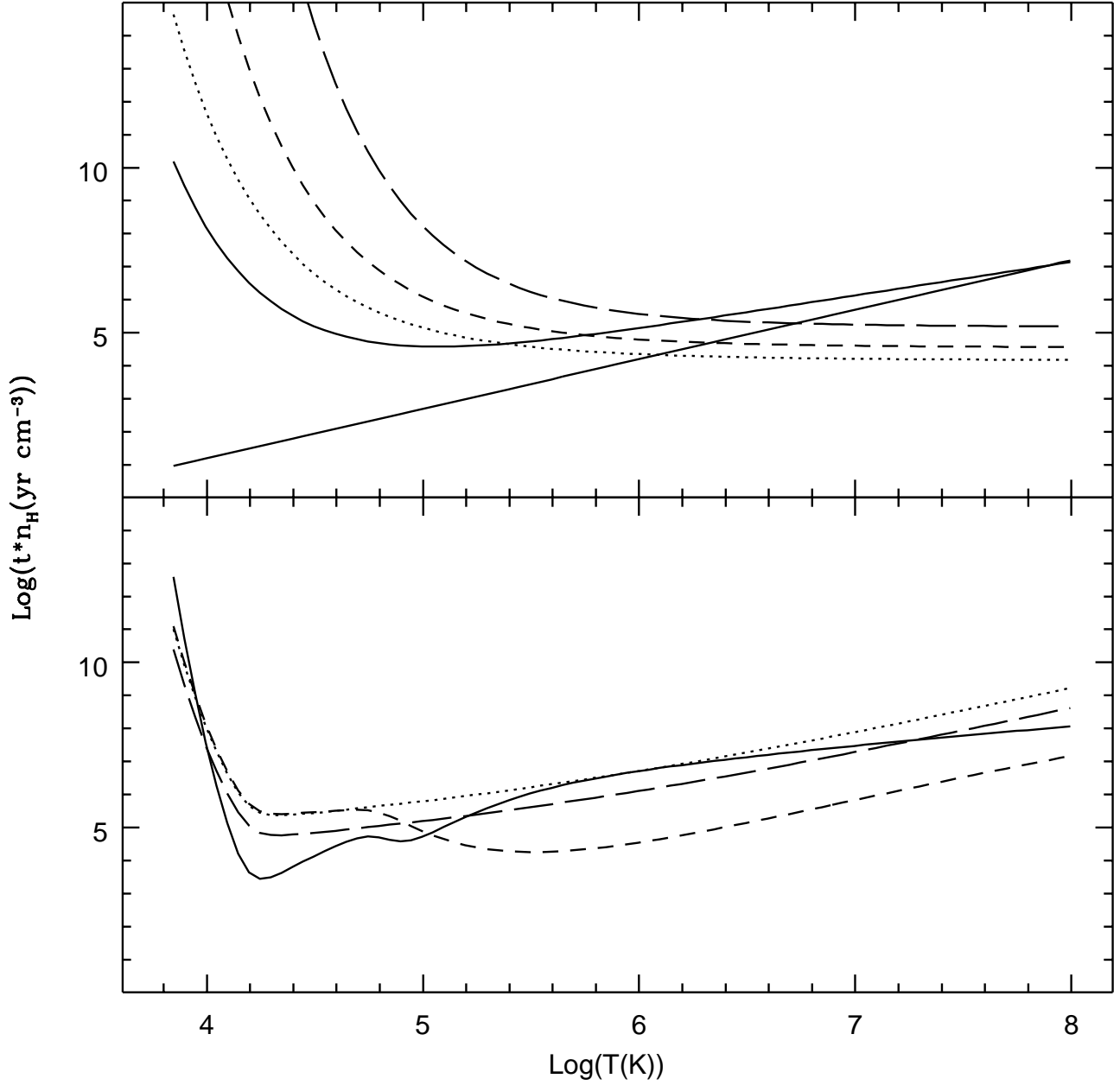


Figure 1: (a) Coulomb equilibration time (straight solid line), cooling time (solid), and collisional ionisation times for HI (dotted), HeI (short-dashed) and HeII (long-dashed) for a primordial plasma with $\Omega_{\text{B}} = 0.05$, $h = 0.5$ and residual ionised fraction taken from Peebles (1993). (b) Cooling time (solid) and recombination times for HII (dotted), HeII (short-dashed) and HeIII (long-dashed) for a primordial plasma with $\Omega_{\text{B}} = 0.05$, $h = 0.5$ and equilibrium ionised fraction.

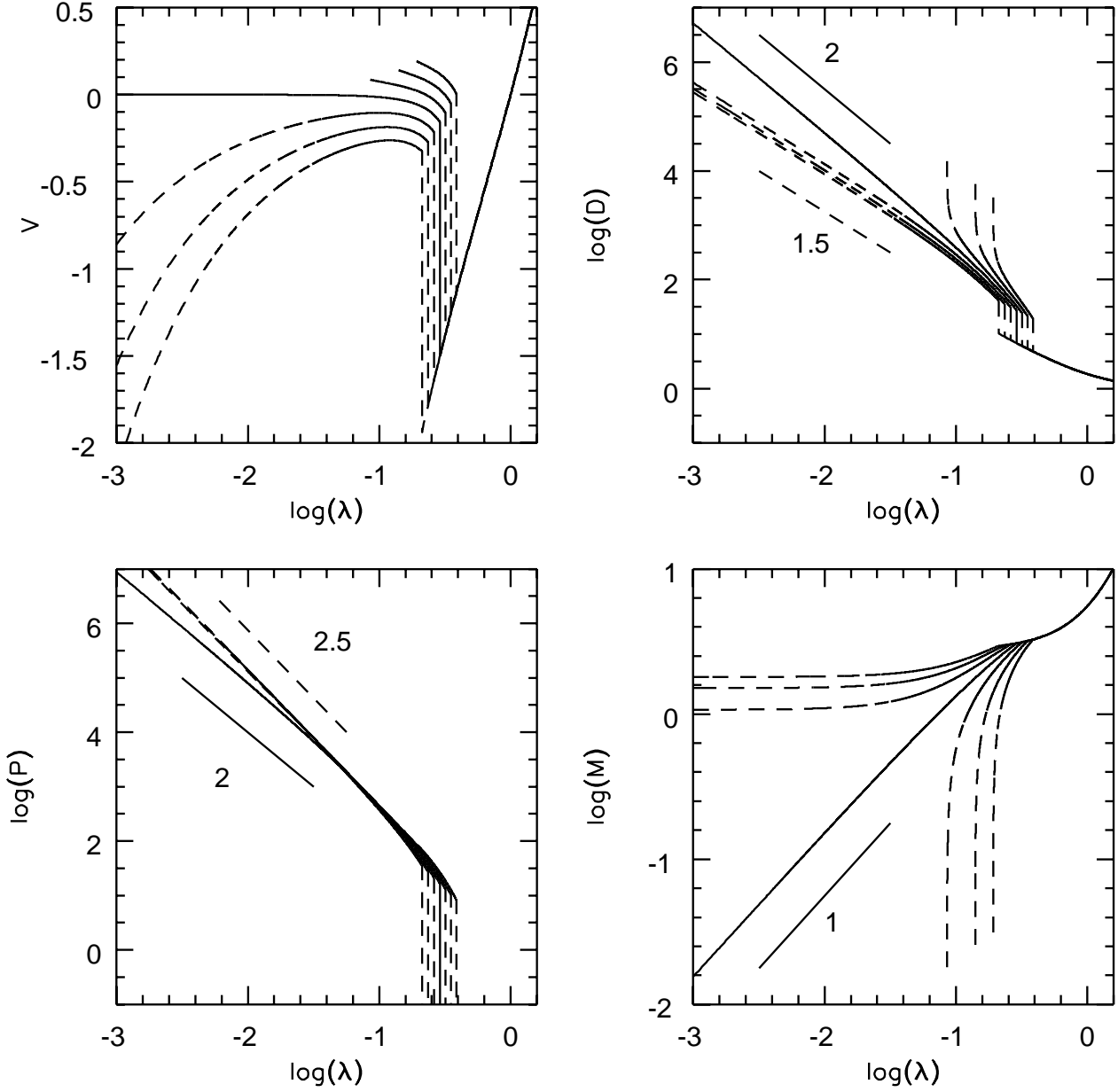


Figure 2: Self-similar velocity (top-left), density (top-right), pressure (bottom-left), mass (bottom-right) profiles for shocked accretion in the case $\epsilon = 2/3$ and $\gamma = 5/3$. Solid line: solution satisfying the inner boundary $V(0) = M(0) = 0$. Dashed lines: solutions with $\lambda_s < \lambda_s^0$ or $\lambda_s > \lambda_s^0$, where λ_s^0 is the position of the shock for the solution plotted in solid line. The expected asymptotic slopes are indicated.

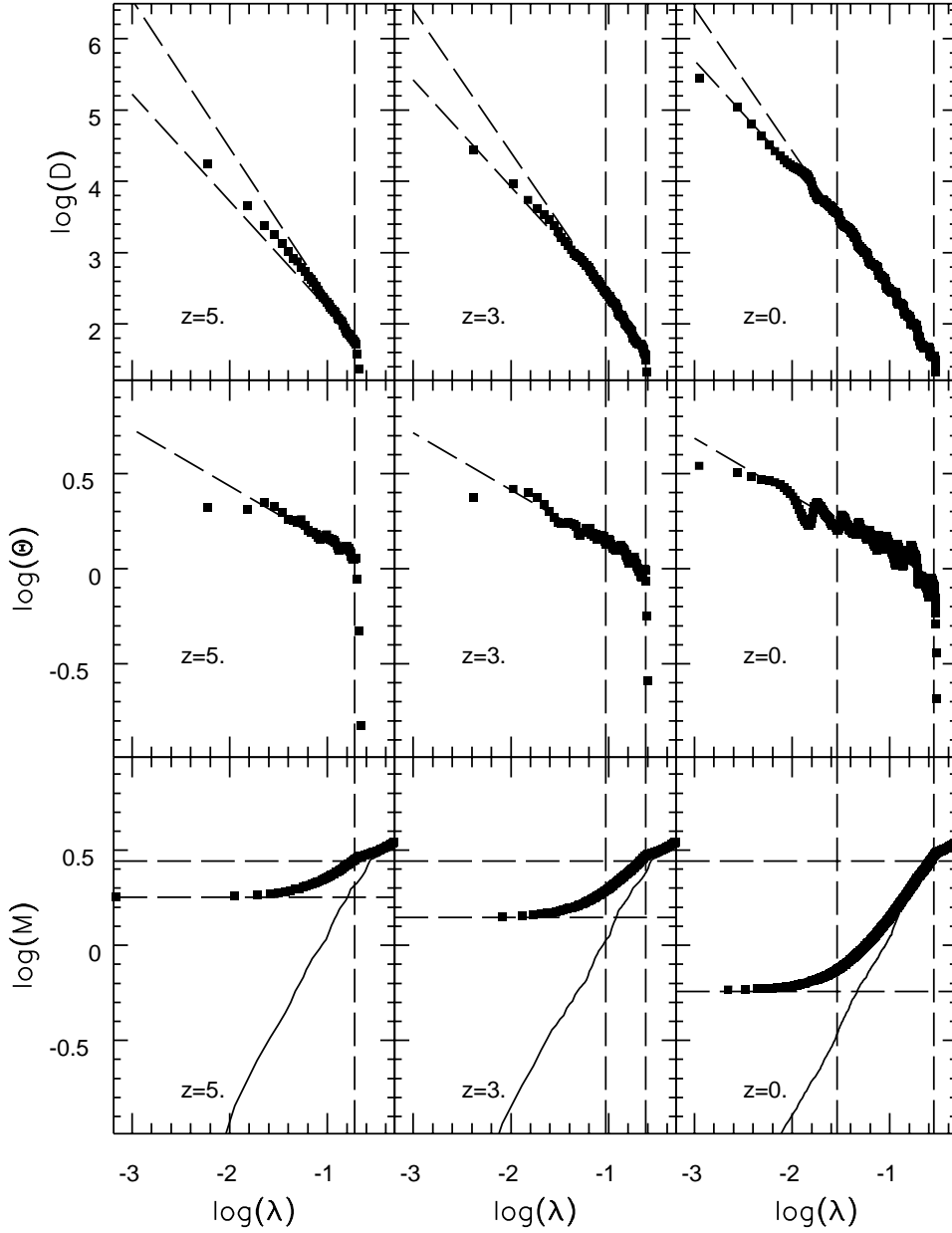


Figure 3: Radial profiles at different redshifts for a halo with $V_c = 220 \text{ km s}^{-1}$. Top: Density. The two slopes plotted are -2 and -1.5. Middle: Temperature. The slope plotted is -0.3. Bottom: Mass. The top horizontal dashed line is the mass of the black hole in the case of cold accretion and the bottom one is the total mass that has cooled below 8000 K. The solid line is the self-similar mass profile in the case of adiabatic collapse. In all cases the left vertical dashed line is the position of the cooling wave and the right one is the position of the shock wave.

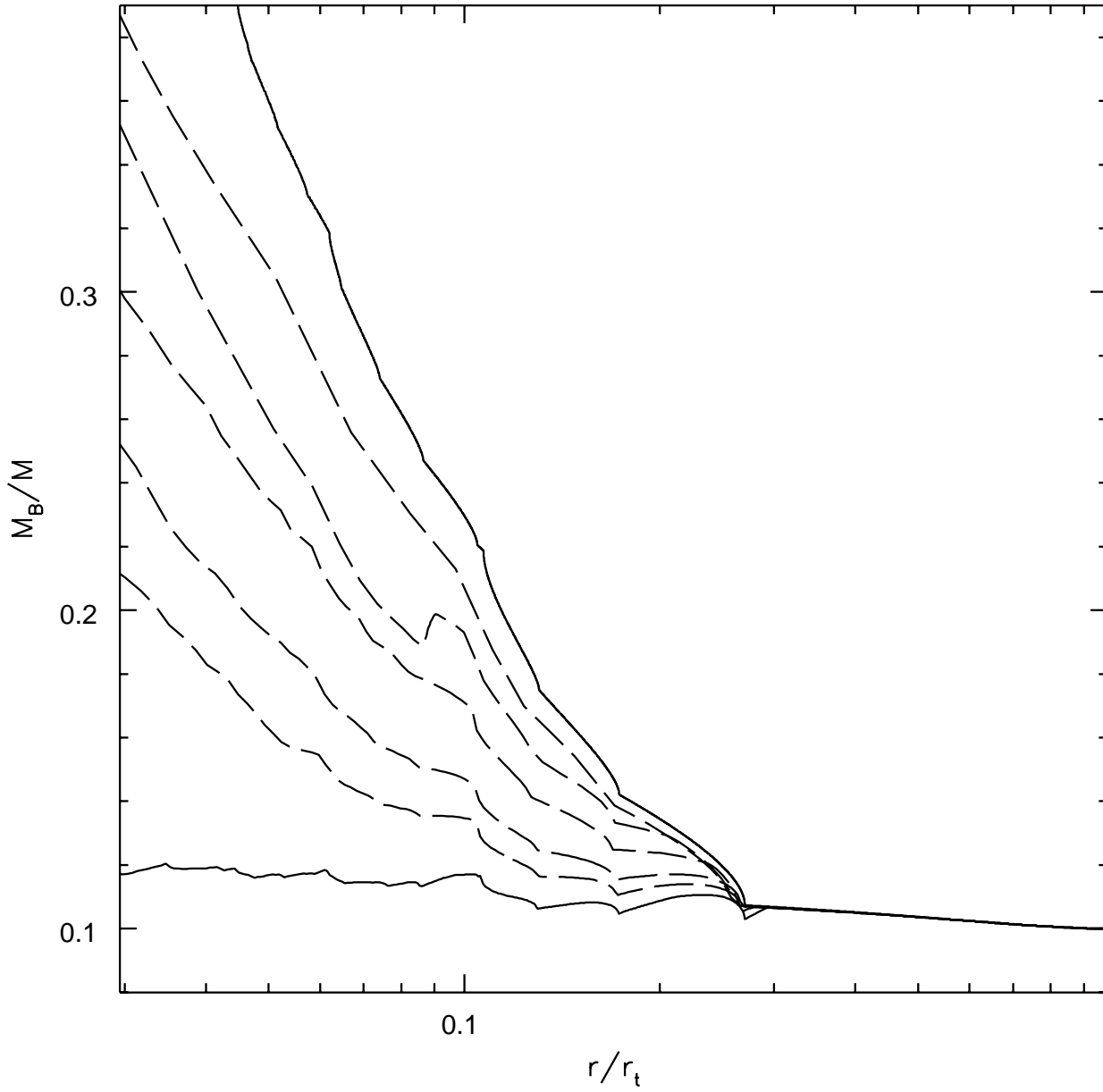


Figure 4: Mass of baryons to total mass ratio versus fraction of the turnaround radius at $z = 0$. In short-dashed line, from left to right one has halos with circular velocity 300, 140, 80, 40 and 20 km s^{-1} . In solid line one has the adiabatic collapse (bottom) and collapse onto a black hole (top). In all cases $\Omega_B = 0.1$.

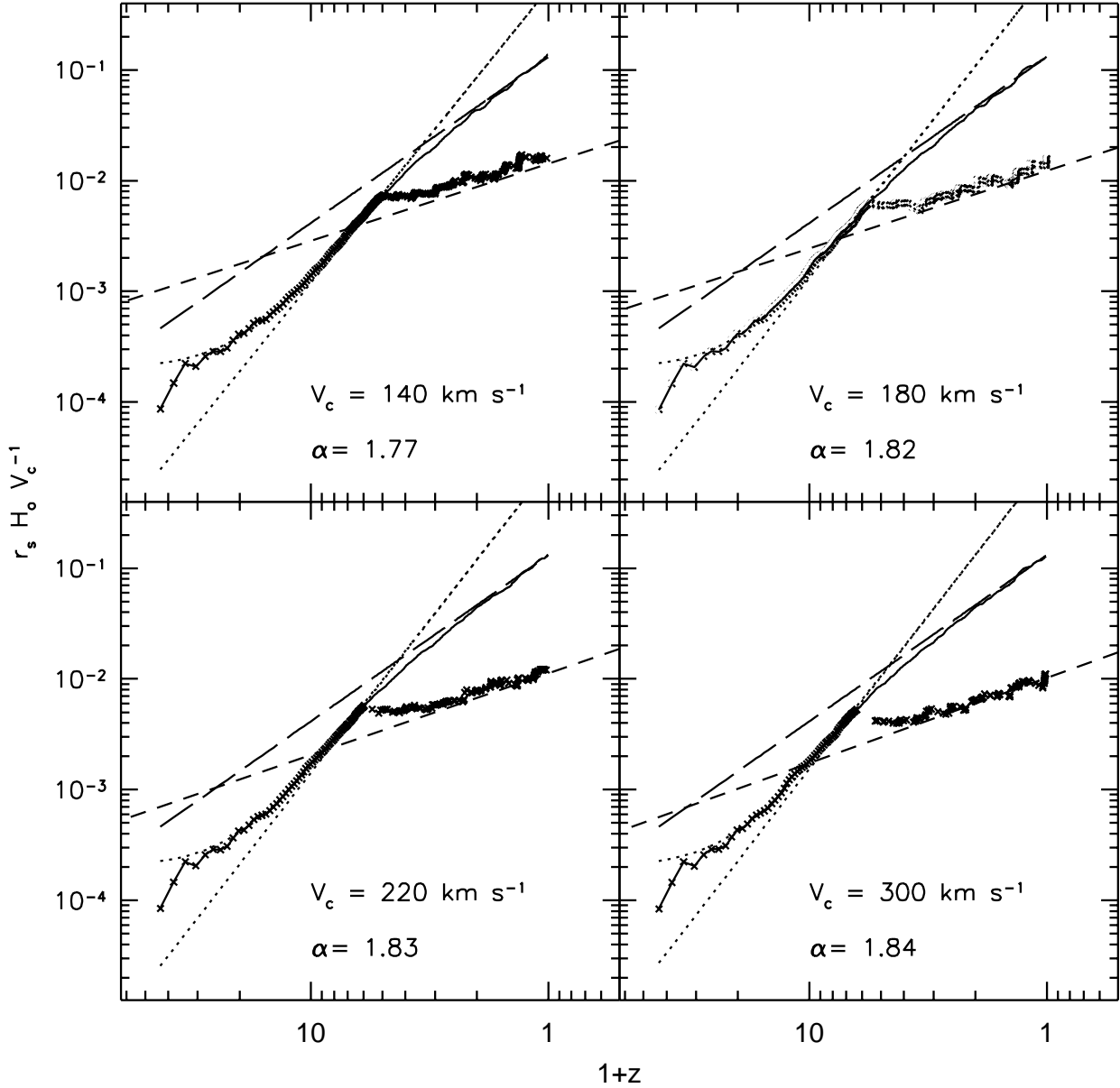


Figure 5: Evolution in time of the shock wave position (solid line) and the cooling wave position (crosses) as given by the numerical simulations for halos with $V_c > 100 \text{ km s}^{-1}$ and $\Omega_B = 0.05$. Long-dashed lines correspond to the adiabatic evolution of the shock. Dotted-lines correspond to a growth in time proportional to t^α , and an off-set equal to the softening parameter. The value of the exponent α is given in each panel. Short-dashed lines correspond to the analytical expression given in equation (6.31).

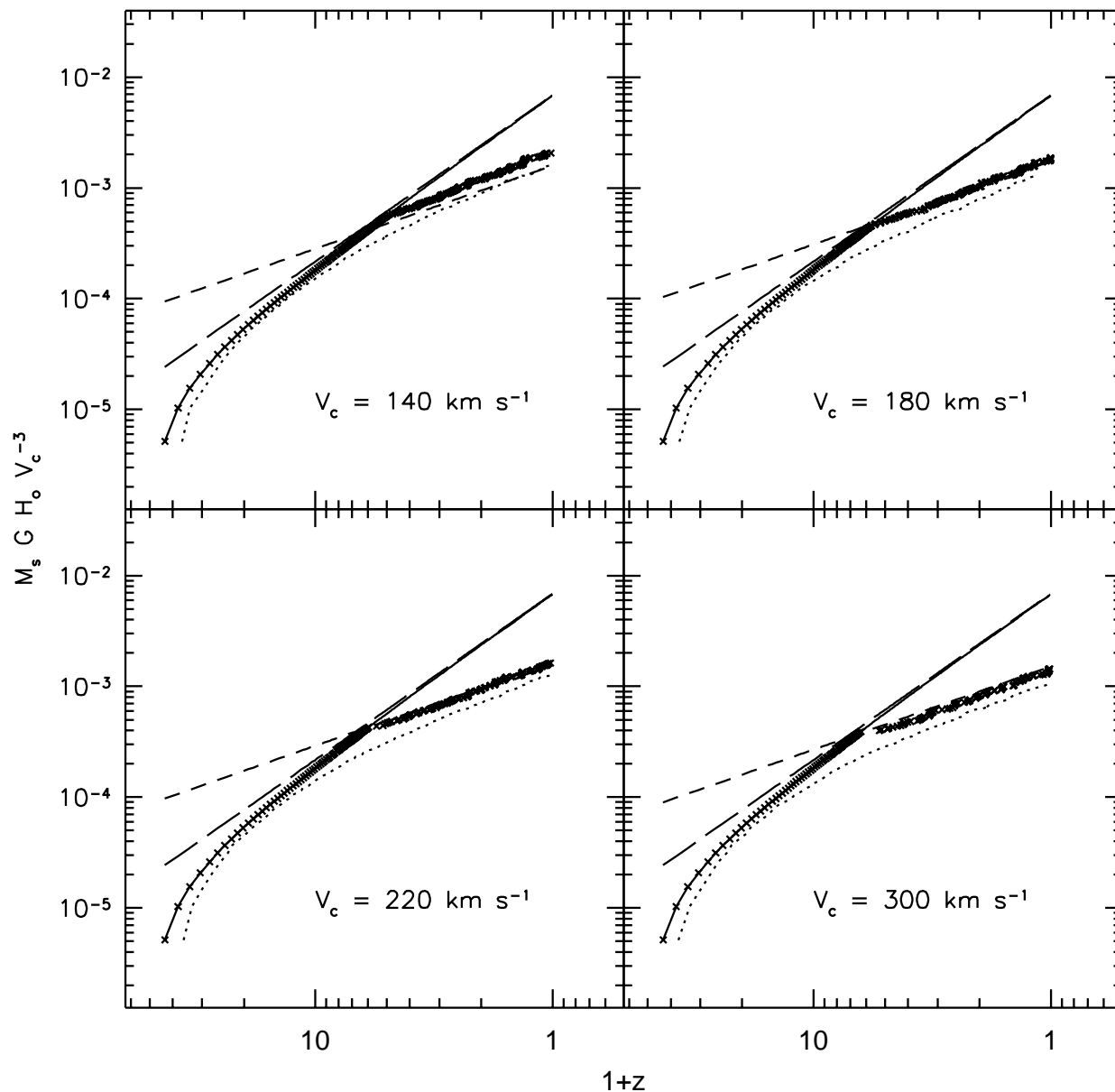


Figure 6: Evolution in time of the gas mass within the shock wave (solid line), the cooling wave (crosses), and the mass that has cooled below 8000 K (dotted line) as given by the numerical simulations for halos with $V_c > 100 \text{ km s}^{-1}$ and $\Omega_B = 0.05$. Long-dashed lines correspond to the adiabatic evolution of the shock. Short-dashed lines indicate a growth in time proportional to $t^{-1/2}$.

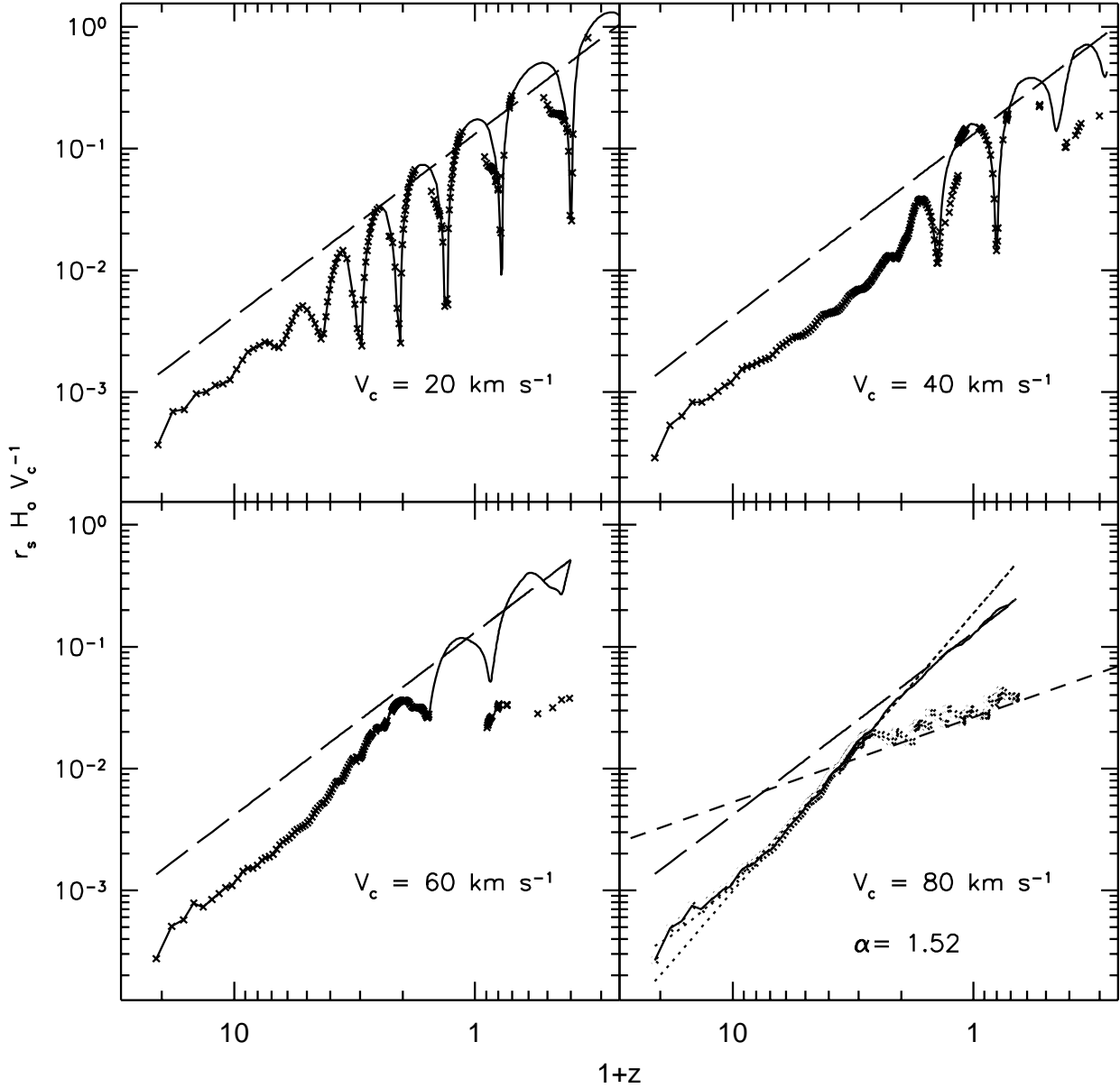


Figure 7: Evolution in time of the shock wave position (solid line) and the cooling wave position (crosses) as given by the numerical simulations for halos with $V_c < 100 \text{ km s}^{-1}$ and $\Omega_B = 0.05$. Long-dashed lines correspond to the adiabatic evolution of the shock. In the bottom right panel the short-dashed line corresponds to the analytical expression given in equation (6.31). The dotted-lines indicate a power-law $t^{1.5}$, with an off-set equal to the softening parameter.

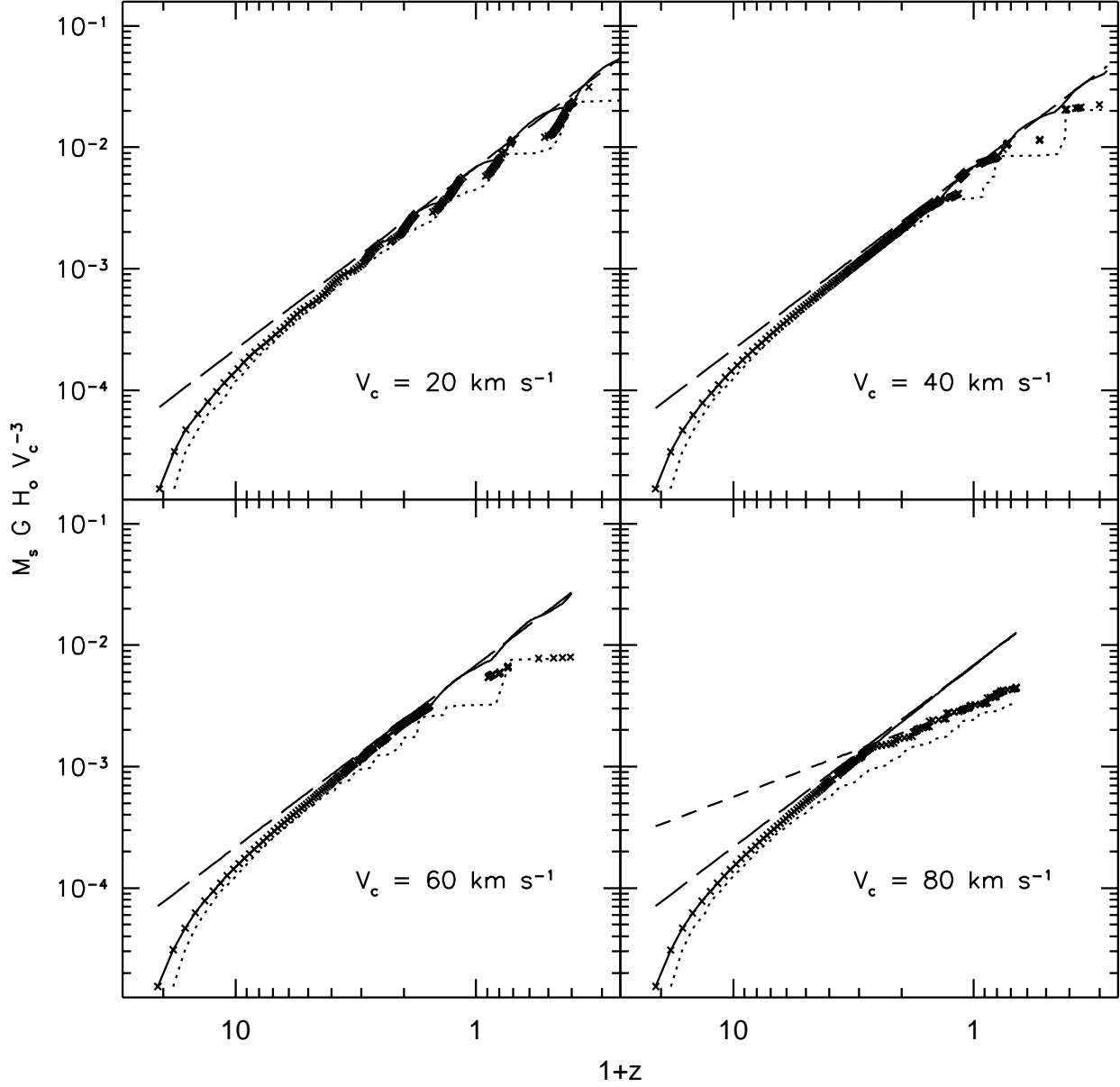


Figure 8: Evolution in time of the gas mass within the shock wave (solid line), the cooling wave (crosses), and the mass that has cooled below 8000 K (dotted line) as given by the numerical simulations for halos with $V_c < 100 \text{ km s}^{-1}$ and $\Omega_B = 0.05$. Long-dashed lines correspond to the adiabatic evolution of the shock. In the bottom right panel the short-dashed line corresponds to a growth in time proportional to $t^{1/2}$.

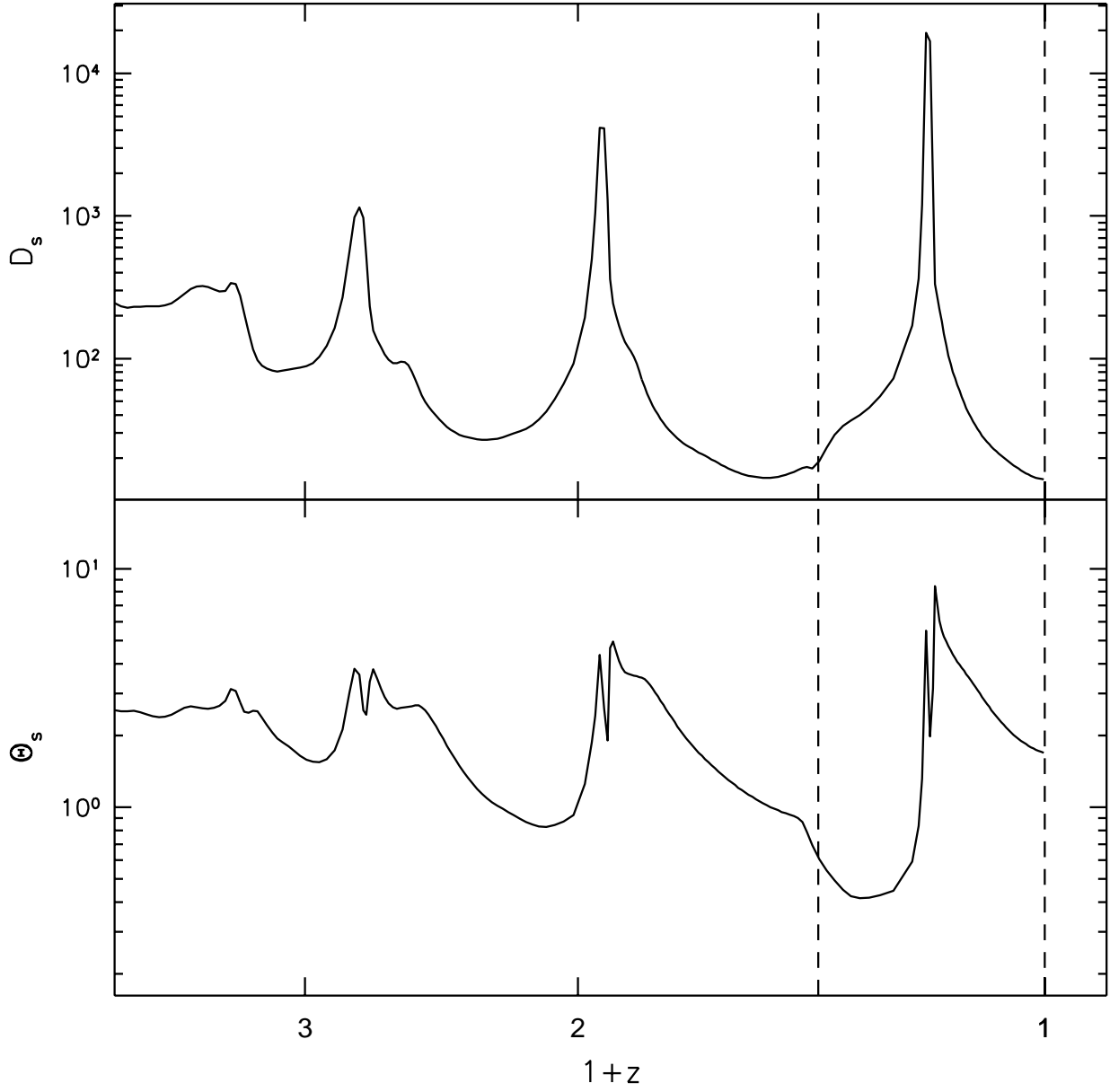


Figure 9: Evolution in time of the post-shock density (top) and the post-shock temperature (bottom) for a halo with $V_c = 40 \text{ km s}^{-1}$ and $\Omega_B = 0.05$. Short-dashed lines indicate the times at which radial profiles are plotted in Figure 6.9.

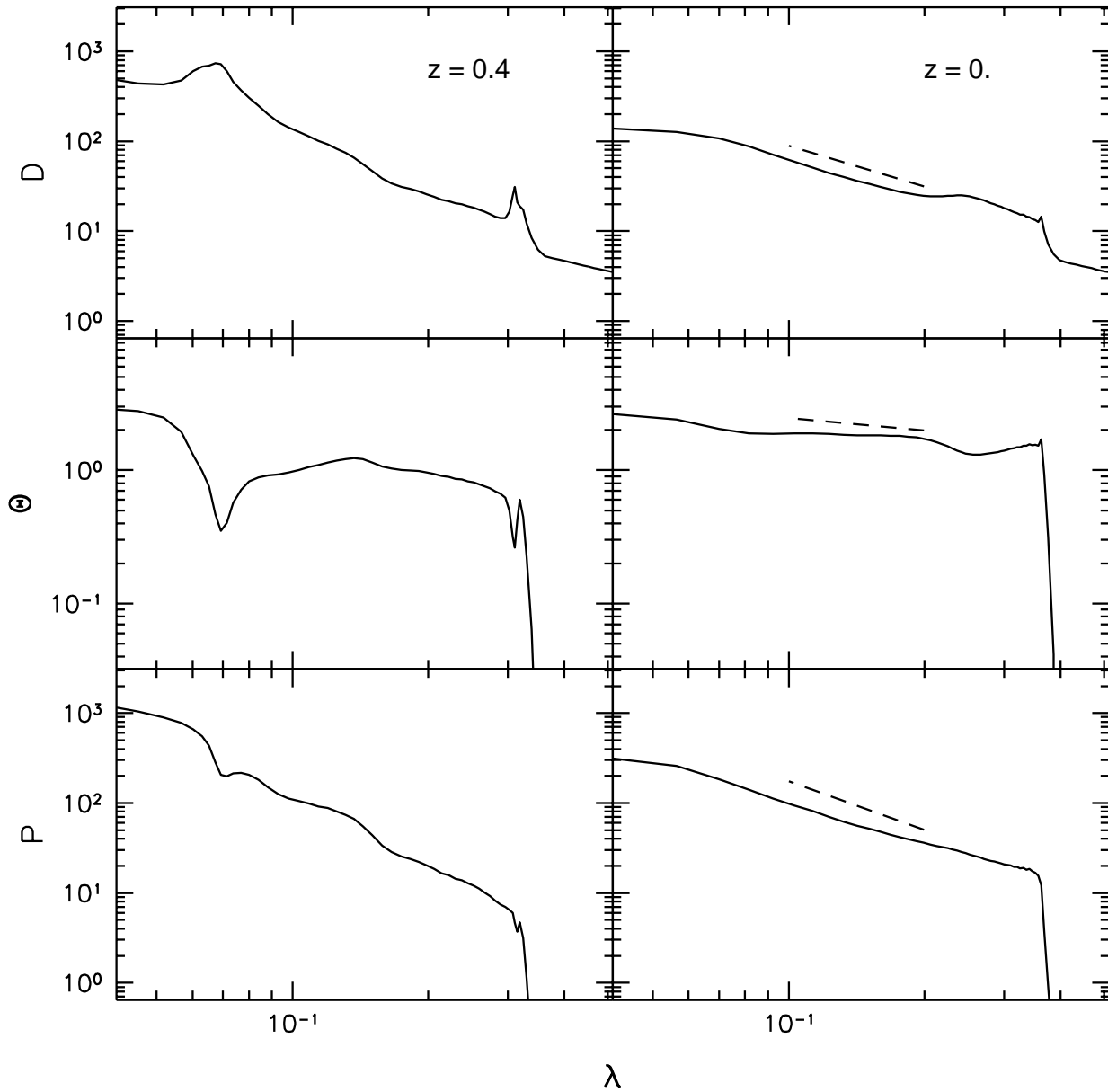


Figure 10: Radial profiles at different redshifts for a halo with $V_c = 40 \text{ km s}^{-1}$ and $\Omega_B = 0.05$. Top: Density. Middle: Temperature. Bottom: Pressure. The left panel is a snapshot taken just after the shock reached maximum expansion. The right panel was taken during the expansion phase. The short-dashed lines indicate the power-law behaviour -1.5 , -0.3 , -1.8 for the density, temperature and pressure respectively.

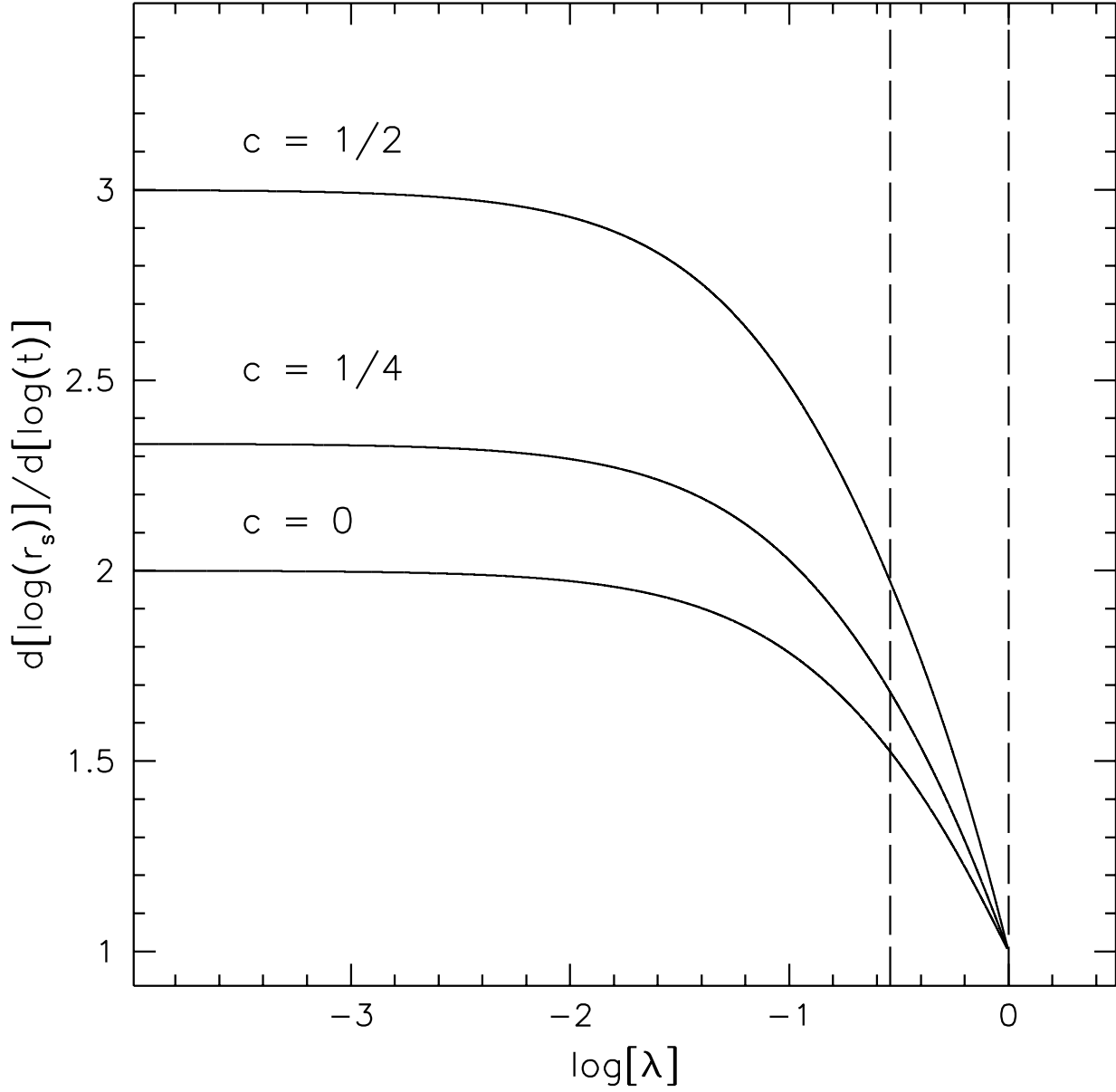


Figure 11: Variation of the slope of $r_s(t)$ with λ for different slopes of the cooling function c in the case $\Omega_B = 1$. The long-dashed lines indicate the position of the nonradiative shock and the turnaround radius.

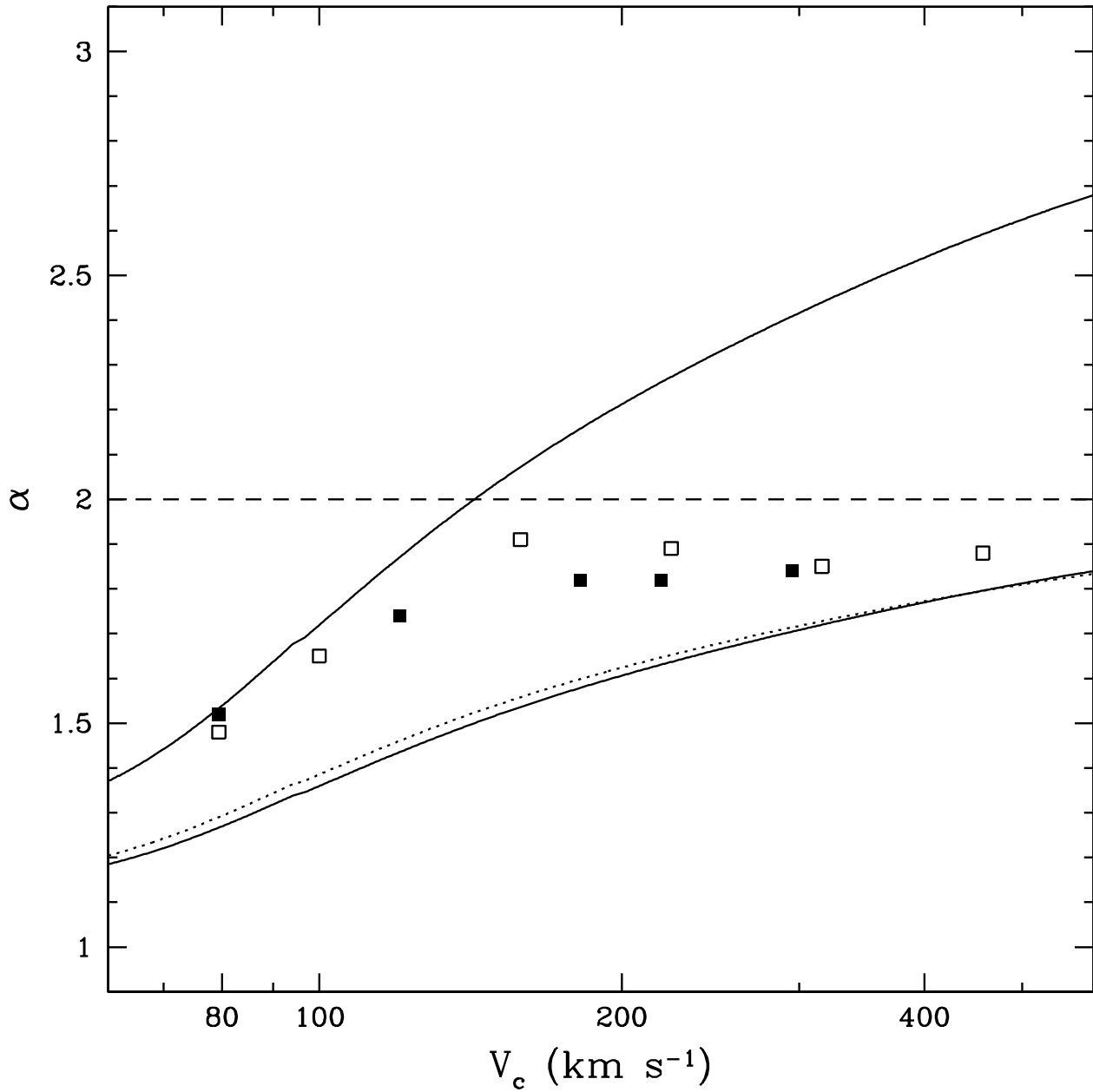


Figure 12: Solid lines: Predicted limits for the power-law evolution in time of the position of a radiative shock $r_s \sim t^\alpha$ in the case two-body process dominate the radiative cooling. The lower limit is the analytical approximation to the numerical limit (dotted line). The short-dashed line is the expected exponent if Compton cooling is the dominant cooling. Filled squares: Fitted exponent to simulations with $\Omega_B = 0.05$. Empty squares: Fitted exponent to simulations with $\Omega_B = 0.1$.

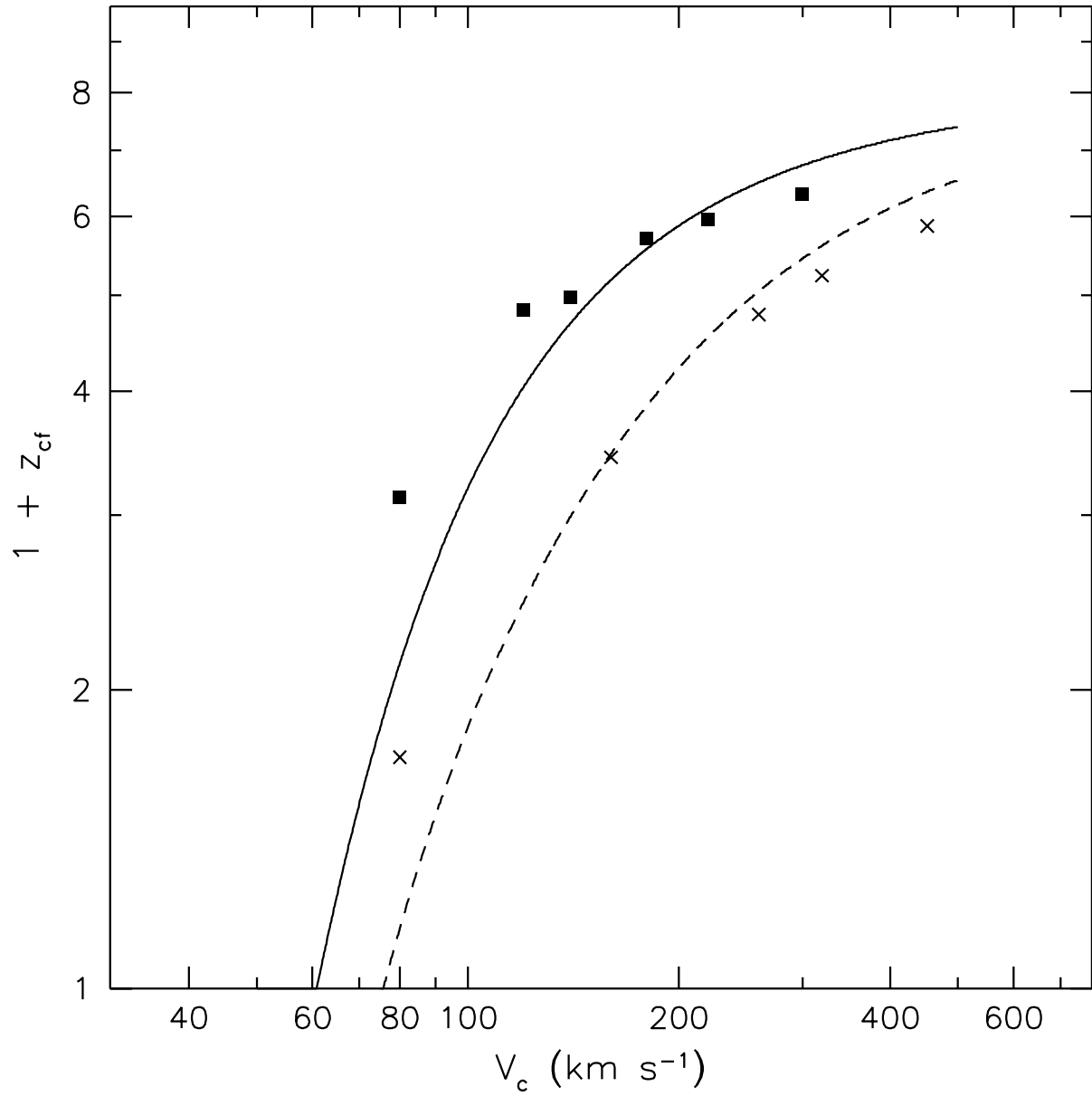


Figure 13: Predicted redshift for the onset of a cooling flow at the central regions of a collapsing halo in a flat universe with a baryonic fraction $\Omega_B = 0.05$ (solid line) and $\Omega_B = 0.1$ (dashed line). Filled squares: numerical simulations with $\Omega_B = 0.05$. Crosses: numerical simulations with $\Omega_B = 0.1$.